Assessment of the mapping of fractional woody cover in southern African savannas using multi-temporal and polarimetric ALOS PALSAR L-band images

Mikhail Urbazaev[a]*, Christian Thiel[a], Renaud Mathieu[b,c], Laven Naidoo[b], Shaun R. Levick[d], Izak P. J. Smit[e,f], Gregory P. Asner[g], Christiane Schmullius[a]

[a] Department of Earth Observation, Institute of Geography, Friedrich Schiller University Jena, Jena, Germany

[b] Ecosystem Earth Observation, Council for Scientific and Industrial Research, Pretoria, South Africa

[c] Department of Geography, Geoinformatics and Meteorology, University of Pretoria, Pretoria, South Africa

[d] Department of Biogeochemical Processes, Max Planck Institute for Biogeochemistry, Jena, Germany

[e] Scientific Services, South African National Parks, Skukuza, South Africa

[f] Centre of African Ecology, School of Animal, Plant and Environmental Sciences, University of Witwatersrand, Johannesburg, South Africa

[g] Department of Global Ecology, Carnegie Institution for Science, Stanford, CA, USA

E-Mails:

mikhail.urbazaev@uni-jena.de;

christian.thiel@uni-jena.de;

rmathieu@csir.co.za;

lnaidoo@csir.co.za;

slevick@bgc-jena.mpg.de;

izak.smit@sanparks.org;

gpa@stanford.edu;

c.schmullius@uni-jena.de

***Corresponding Author:**

Mikhail Urbazaev

Email: mikhail.urbazaev@uni-jena.de

Tel: +49 3641 94 88 85

Fax: +49 3641 94 88 82

Abstract

Woody vegetation cover affects several ecosystem processes including carbon and water cycling, energy fluxes, and fire regimes. In order to understand the dynamics of savanna ecosystems, information on the spatial distribution of woody vegetation over large areas is needed. In this study we sought to assess multi-temporal ALOS PALSAR L-band backscatter to map woody cover in southern African savannas. The SAR data were acquired from the JAXA archive, covering various modes and seasons between 2007 and 2010. We used high resolution airborne LiDAR data as reference data to interpret SAR parameters (including backscatter intensities and polarimetric decomposition components), to develop SAR-based models as well as to validate SAR-based woody cover maps. The LiDAR survey was carried out in April 2008 with the Carnegie Airborne Observatory (CAO, http://cao.ciw.edu). The highest correlations to the reference data were obtained from SAR backscatters of the dry season, followed by the wet season, and the end of the wet season. The volume components from polarimetric decompositions (Freeman-Durden, Van Zyl) were calculated for the end of wet season, and showed similar correlations to the LiDAR data, when compared to cross-polarized backscatters (HV). We observed increased correlation between the SAR and LiDAR datasets with an increase in the spatial scale at which datasets were integrated, with an optimum value at 50 m. We modeled woody cover using three scenarios: (1) a single date scenario (i.e., woody cover map based on a single SAR image), (2) a multi-seasonal scenario (i.e., woody cover map based on SAR images from the same year and different seasons, based on key phonological difference), and (3) a multi-annual scenario (i.e., woody cover map based on SAR data from different years). Predicted SAR-based woody cover map based on Fine Beam Dual Polarization dry season SAR backscatters of all years yielded the best performance with an R^2 of 0.71 and RMSE of 7.88%. However, single dry season SAR backscatter achieved only a slightly lower accuracy (R^2=0.66, RMSE=8.45%) as multi-annual SAR data, suggesting that a single SAR scene from the dry season can also be used for woody cover mapping. Moreover, we investigated the impact of the number of samples on the model prediction performance and showed the benefits of a larger spatially explicit LiDAR dataset compared to much

smaller number of samples as they can be collected in the field. Collectively, our results demonstrate that L-band backscatter shows promising sensitivity for the purposes of mapping woody cover in southern African savannas, particularly during the dry season leaf-off conditions.

Keywords: L-band, backscatter, ALOS PALSAR, savanna, woody cover, Carnegie Airborne Observatory, LiDAR, seasonality

1. Introduction

In the age of accelerating global change the ability to measure changes in the Earth's ecosystems is crucial. This is especially needed in African savannas, which are predicted to be heavily affected by climate and land use changes (Marchant 2010; Sankaran et al. 2005). Due to the simultaneous occurrence of patches of trees, shrubs and grasses (Scholes and Archer 1997) and pronounced seasonal variations driven by water availability (Venter et al. 2003), savannas are very heterogeneous, dynamic and sensitive ecosystems. Changes in air temperature and precipitation intensities may have a significant impact on the tree-grass balance (e.g., Kulmatiski and Beard 2013) as may increasing atmospheric CO_2 (Buitenwerf et al. 2012). A shift in this balance can cause a conversion of savannas into forests or grasslands (Sankaran et al. 2004), that would impact severely on biodiversity and the livelihood of local rural communities. The spatial distribution of woody cover in savannas and its temporal dynamics are determined by available resources (water and nutrients) and disturbance events (fire, herbivory and human) (Coughenour and Ellis 1993; Sankaran et al. 2005), with varying effects depending on the scale (from hillslope catena to region). In turn, it affects carbon and water cycles, fire regimes, nutrient cycling and soil erosion (Scholes and Archer 1997). Field measurements of woody cover, defined as the area vertically projected on a horizontal plane by woody plant canopies (Jennings et al. 1999), are associated with high costs (e.g. labor intensive and time consuming) and are limited to point measurements, which cannot adequately describe patterns at different spatial scales. Information on the spatial distribution of woody vegetation provides local stakeholders with important baseline data for the development of sustainable management strategies as well as assessing the effects of

management decisions (e.g., fire and animal controls) (Bucini et al. 2010). Furthermore, these products can help provide a better understanding of the ecosystem dynamics and the effects of environmental drivers through modeling.

One of the biggest challenges of mapping woody cover using optical datasets is to distinguish between woody and non-woody (herbaceous) vegetation layers (Bucini et al. 2010). Since they often have similar spectral properties, it is only possible to separate these vegetation types by using either hyperspectral data (Lu 2006) or time specific optical data capitalizing on phenological differences between these two plant growth forms (Loveland et al. 2000), see for example the Australian Statewide Landcover and Trees Study (SLATS) initiative (Armston et al. 2009) and the Australian National Carbon Accounting System - Land Cover Change Program (NCAS-LCCP) (Lehmann et al. 2013). These examples rely on the effective contrast between woody and grassy vegetation during a relatively long dry season, devoid of clouds, and when most woody canopies remain green (evergreen) while the grassy understory is dry. In large parts of the semi-arid savanna landscapes in southern Africa, trees are deciduous and shed their leaves during the dry season (winter), while both grass and woody vegetation are green during the wet season (summer). Maximum "green" contrast between both life-forms occurs during the autumn (drying) and spring (wetting), when grasses senesced first and when trees flushes before the first rains, respectively (Zeidler et al. 2012). However, these periods are short (one month), variable across years, and plagued by spatial phenological heterogeneity controlled by high rainfall and soil variability (Venter et al. 2003). Thus these short windows are not easy to target for a consistent woody cover mapping using optical imagery. Furthermore, accuracy assessments of the global operational tree cover product (MODIS VCF (Hansen et al. 2005)) showed clear limitations in regions with low tree cover (e.g., tundra-taiga transition zone (Montesano et al. 2009)).

Alternatively, the estimation of woody cover parameters is possible with radar sensors. Microwaves operate in the spectral range between 1 cm and 1 m and are particularly useful for weather independent applications, as long wavelengths penetrate clouds. A key parameter obtained from synthetic aperture

radar (SAR) data, is the backscatter intensity. This SAR parameter measures the return energy from a ground object and is determined by the physical (geometry of the object) and electrical (dielectric constant, which is mostly determined by the water content) properties of the reflective material, as well as by the frequency, polarization and angle of incidence of the emitted wave (Raney 1996). The interactions of the radar waves with vegetation elements are determined by their size and shape. Short waves (X-, C-band) interact primarily with "small" vegetation parts (leaves, twigs) and long waves (L-, P-band) with "large" parts (branches, trunks) (Chauhan et al. 1991; Le Toan et al. 1992; Lucas et al. 2004), suggesting that longer wavelengths such as L-band would be more suitable for the retrieval of woody vegetation structure parameters (e.g., stem volume, aboveground biomass (AGB)) (Kasischke et al. 1997). Since microwaves, especially when using long wavelengths, interact primarily with branches and trunks, they are less sensitive to the grass layer, which should help to separate woody and non-woody vegetation layers. Further, density of branches and trunks are closely related with woody canopy cover, suggesting that L-band data would be appropriate for woody cover modeling. The polarization of the microwave also affects the backscatter mechanisms of vegetated targets. The interaction of vertically polarized waves is generally higher with vertically oriented elements (branches, trunks), as the interaction of horizontally polarized waves is higher with horizontally oriented objects (leaves, twigs) (Leckie and Ranson 1996). The cross-polarized (HV) waves are more sensitive to volume scattering (e.g. as occurring within woody canopies) as opposed to co-polarized (HH, VV) waves (Rauste et al. 1994; Watanabe et al. 2006). Full polarimetric datasets (i.e. all linear polarizations HH, HV, VH and VV) are now available from recent satellite SAR sensors, e.g. ALOS PALSAR and PALSAR-2, or RADARSAT-2. Target scattering processes can be modeled and quantified from the decomposition of such data. Incoherent target decomposition theorems, derived from second-order scattering matrices, are used for describing scattering processes in vegetated areas. Such model-based incoherent decomposition theorems decompose a full polarimetric dataset into three basic scattering processes (e.g., Freeman and Durden 1998; van Zyl 1989): surface scattering, double bounce, and volume scattering. The use of polarimetric decompositions should contribute to improve

the modeling of the scattering mechanisms of heterogeneous vegetation objects (trees and shrubs) (Freeman and Durden 1998; Lee and Pottier 2009). It is hypothesized that the volume component should more directly relate to the canopy scattering and thus should be more sensitive to woody cover than single polarized bands.

In southern African savannas, which seldom reach canopy closure, AGB is closely linked to a combination of height and woody cover (Colgan et al. 2012). Thus the findings from previous studies relating AGB and L-band backscatter are relevant in this context. Mitchard et al. (2009) estimated AGB of tropical savannas and woodlands across four different African landscapes using ALOS PALSAR L-band backscatter. Despite the different vegetation structure across four test sites the authors reported consistent and similar relationships between field-based AGB estimates and HV backscatter with R^2 varying between 0.61 and 0.76 with a clear reduction in sensitivity between 150 and 200 Mg/ha. Due to a stronger impact of soil moisture and roughness on HH backscatter, the correlation between HH data and AGB was significantly lower compared to cross-polarized data. The authors concluded that L-band backscatter data can be used to map AGB up to 150 Mg/ha at high accuracies (~±20%), what especially suitable for tropical savannas and woodlands. Carreiras et al. (2012) mapped AGB in heterogeneous vegetation areas of Guinea-Bissau with 2008 ALOS PALSAR mosaic at 50 m spatial resolution. The vegetation in the study area is characterized by closed and open tropical rainforest, mangroves as well as savanna woodlands. The results can be summarized as follows: HV backscatter data showed a stronger correlation to the field-based AGB estimates than HH; saturation level occurred at around 100 Mg/ha; the machine learning algorithm (bagging stochastic gradient boosting (BagSGB) after Breiman et al. (1984)) achieved much higher retrieval accuracy than a semi-empirical regression with a coefficient of correlation (R) of 0.95 vs. 0.33 and RMSE of 26.62 Mg/ha vs. 66.46 Mg/ha, respectively. Ryan et al. (2012) detected small-scale deforestation and forest degradation in woodlands of central Mozambique using multi-temporal ALOS PALSAR data acquired during the dry season in combination with field-based AGB estimates.

Until now there has been limited exploration of woody cover mapping with SAR imagery in woodlands, shrublands and savannas across the world, particularly in southern Africa. In a semi-arid rangeland of Jornada del Muerto, New Mexico Musick et al. (1998) examined the potential of airborne SAR data acquired at different frequencies (C-, L-, and P-bands) to map woody shrub density. In this environment where mature shrubs consist mostly of stems of intermediate size (diameter of 1-3 cm), L-HV backscatter was found to produce the highest correlation with woody shrub density, in agreement with simulation results reported by Ferrazzoli and Guerriero (1995). Lucas et al. (2006) showed that C-band data are well related to the Landsat-derived Foliage Projected Cover product and can be used to map foliage projected cover in savannas and open woodlands of Northern Australia. Bucini et al. (2010) used single polarimetric L-band data (HH polarization) from the Japanese Earth Resources Satellite 1 (JERS-1) in combination with optical Landsat ETM+ imagery for mapping woody cover for the two million hectares of Kruger National Park. JERS-1 L-band backscatter was the most important variable in the prediction model for woody cover, followed by the Landsat green channel (Bucini et al. 2010). Mathieu et al. (2013) mapped total canopy cover using multi-temporal full polarimetric RADARSAT-2 C-band imagery and airborne LiDAR data in the southern African Lowveld savannas. The woody cover product generated at a spatial resolution of 105 m was validated with a coefficient of determination (R^2) of 0.71 and root mean square errors (RMSE) of 8.1%.

L-band has been successfully used to map fractional woody cover (Bucini et al. 2010; Li et al. 2012; Musick et al. 1998) as well as regional or global forests (Dong et al. 2014; Shimada et al. in press). With the successful launch of the fully polarimetric Advanced Land Observation Satellite's Phased Array L-band Synthetic Aperture Radar (ALOS PALSAR, successor of JERS-1) in 2006, opportunities for accurate mapping of woody vegetation have been increased with the addition of cross-polarized bands (HV) (Kasischke et al. 1997; Le Toan et al. 1992; Rignot et al. 1994). To the author's knowledge there had been no comprehensive investigation of the performance of multi-temporal and polarimetric L-band SAR imagery for mapping fractional woody cover in African savannas; this gap

needs to be addressed, especially in the context of the new and upcoming L-band sensors (ALOS-2, DESDynI-R, Tandem-L, NISAR, SAOCOM).

Here we examined the potential of multi-temporal full, dual and single polarimetric ALOS PALSAR L-band data for mapping fractional woody cover in southern African savannas. Airborne Light Detection and Ranging (LiDAR) data served as reference data for interpreting SAR data and developing SAR models. From a set of multi-season and multi-year ALOS PALSAR images backscatter intensities as well as polarimetric decompositions were extracted and correlated against LiDAR-based woody cover reference data. In this study we first investigated the optimum (1) season, (2) L-band polarimetric SAR products (backscatter and polarimetric decompositions), and (3) spatial resolution or scale of analysis for the fractional woody cover mapping. The optimal channel combination, season and spatial resolution were determined and several single date or multi-temporal modeling scenarios were assessed for mapping the woody cover. Finally, to examine the impact of the number of samples used for model calibration on the model prediction performance, we modeled woody cover with different number of samples selected using a random stratified approach from the LiDAR data. Our purpose was to quantify the benefits of a larger spatially explicit LiDAR dataset compared to typically much smaller sample sizes as they can be practically collected in the field, and to assess the number of samples required to reach a given performance for the woody cover retrieval.

2. Study area

The study area is located in the Lowveld in the north-east of the Republic of South Africa and is shown in Fig. 1 together with the ALOS PALSAR footprints of Fine Beam Single Polarization (FBS), Fine Beam Dual Polarization (FBD), and Polarimetry (PLR) modes. The study area extends approximately over 365,000 ha and is divided into three dominant land uses. The largest part (260,000 ha, ca. 70% of total area) is the Kruger National Park (KNP), the largest national conservation area in the country managed by the South African National Parks. Adjacent to KNP is the Sabi Sand Game Reserve (SSGR), managed privately by an association of free-hold owners (60,000 ha, ca. 16% of total area).

Finally the smallest land use within the SAR footprints is the communal lands of the Bushbuckridge Municipality (36,000 ha, ca. 10% of total area), where rural communities make a livelihood from small-scale subsistence agriculture and extraction of natural resources from surrounding savannas and woodlands (e.g. grass for livestock, fuel wood).

The study area is a low-lying and gently undulating landscape with an average elevation of about 400 m and a slight declining gradient toward the east. The slope ranges between 0 and 42.6 degree with a mean slope of 1.71 degree and a standard deviation of 1.74 degree. The regional climate is characterized by high summer air temperatures and a mild, frost-free winter. The average annual temperature is 22 °C. Because of high air temperature and humidity in the summer, the atmosphere is unstable and leads to strong convective rainfall events mostly between October and May (Venter et al. 2003). The dry season extends accordingly between late May and late September. Average annual precipitation in the KNP follows a north-south gradient with 300-500 mm in the north and 500-700 mm in the south (Venter et al. 2003).

The KNP is divided into two broad-scale geological units (Fig. 1). Granite substrates are dominant in the western parts of the KNP and are associated with nutrient-poor soils (moderately deep to shallow coarse sand and loam on upland and duplex soils on bottomlands). The grass layer is mostly wiry, unpalatable and sparse. Granitic landscapes are well wooded with a woody cover varying between 20 and 60% (Bucini et al. 2010; Eckhardt et al. 2000). Basalt substrates occur mostly in the eastern half of the park. Soils are more fertile (dark vertic clay soils) and support high-bulk grasses of high nutritious value. The denser grass layer induces more frequent fires of higher intensity (Smit et al. 2013), which in turn reduce the density of woody plants.

3. Methods and Material

3.1 Remote sensing data

3.1.1 SAR data

ALOS PALSAR was a fully polarimetric L-band (23.6 cm wavelength) sensor and emitted/received in up to four different polarizations (HH, HV, VH and VV) depending on the imaging mode. The mission was terminated in May 2011, after a power failure which could not be recovered. The revisit period was 46 days for imagery taken in the Fine Beam and Polarimetric modes (Rosenqvist et al. 2004). For this work four scenes were available for both the Fine Beam Single Polarization (FBS) and Fine Beam Dual Polarization (FBD) modes, and two for the Polarimetry mode (PLR). The characteristics of the datasets used (acquisition date, polarization, incidence angle, track and frame information) are presented in Table 1. All images were taken on an ascending orbit at around 21:00 local time.

Table 1: Characteristics of the ALOS PALSAR datasets considered in this study and four-days (at image acquisition date and three days before) sum of precipitation for four weather stations located in Kruger National Park

Acquisition mode	Acquisition date	Polarization	Incidence angle [°]	Track	Frame	Precipitation (mm)	Season
FBS	03/02/2007	HH	34.3	586	6680	SKZ: 6.9	MWET
FBS	08/02/2009	HH	34.3	586	6680	SKZ: 10.2	MWET
FBS	27/12/2009	HH	34.3	586	6680	-	MWET
FBS	11/02/2010	HH	34.3	586	6680	SKZ: 0.2	MWET
FBD	06/08/2007	HH/HV	34.3	586	6680	-	DRY
FBD	23/09/2008	HH/HV	34.3	586	6680	SKZ: 0.4	DRY
FBD	11/08/2009	HH/HV	34.3	586	6680	-	DRY
FBD	29/09/2010	HH/HV	34.3	586	6680	-	DRY
PLR	14/04/2007	HH/HV/ VH/VV	21.5	582	6690	NHL: 12.0 SKZ: 13.2	EWET
PLR	19/04/2009	HH/HV/ VH/VV	21.5	582	6690	-	EWET

H horizontal polarization; V vertical polarization; FBS Fine Beam Single Polarization mode; FBD Fine Beam Dual Polarization mode; PLR Polarimetry mode. Weather stations acronyms: NHL: Nhlanguleni; SKZ: Skukuza; TAL: Talamati; TSH: Tshokwane. DRY dry season; EWET end of wet season; MWET middle of wet season.

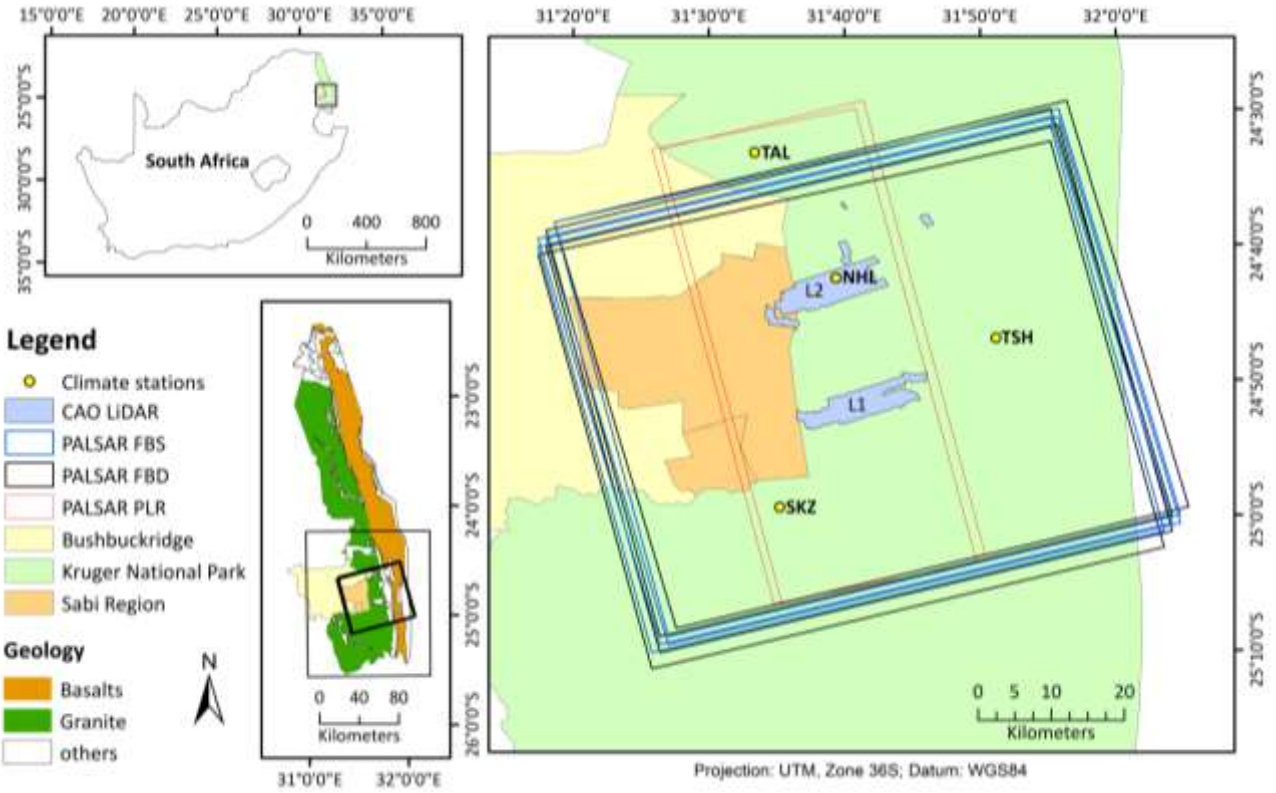

Figure 1: Study area with the ALOS PALSAR footprints in Fine Beam Single Polarization (FBS), Fine Beam Dual Polarization (FBD) and Polarimetry (PLR) modes used in this study (Weather stations acronyms: NHL: Nhlanguleni; SKZ: Skukuza; TAL: Talamati; TSH: Tshokwane)

The datasets in FBD and FBS modes cover the same area, approximately 60 x 70 km, while the two fully polarimetric datasets cover a smaller area (25 x 60 km) located within the FBS/FBD scenes (Fig. 1). The PALSAR data were acquired in the dry season (DRY) or winter (August/September), the middle of rainy season (MWET) or summer (December-February) as well as at the end of rainy season (EWET) or autumn (April). All images used in this study were extracted from the ALOS PALSAR archive. Due to the global acquisition strategy implemented by JAXA the various modes available were biased in term of seasonal coverage (Rosenqvist et al. 2004): for instance, during the MWET season only images in FBS mode were available, during the DRY season only FBD mode, and during the EWET season only PLR mode, respectively. However, a HH dataset was available at each season allowing the investigation of the optimum season to map the woody cover. Further, the best

configuration reported to map the woody cover using RADARSAT-2 (C-band) in the region (winter, HH/HV) (Mathieu et al. 2013) was available.

3.1.2 LiDAR data

LiDAR-based products (e.g., Digital Elevation Model (DEM), Canopy Height Model (CHM)) can be produced with very high accuracy, leading to rapid growth in the use of LiDAR systems in the last ten years (Lefsky et al. 2002). Since LiDAR is usually operated from an aerial platform, its use is limited to small spatial coverage due to high costs, and as a result, the main field of application is restricted to local scales. An aerial LiDAR platform can be used efficiently to provide a large number of reference data for robust SAR-based modeling (e.g., Cartus et al. 2012; Englhart et al. 2011).

Small-footprint discrete-return LiDAR data acquired by the "Carnegie Airborne Observatory" (CAO) Alpha system (Asner et al. 2007) were used in the study as calibration and validation data for the SAR models. The LiDAR data were collected over two areas totaling about 11,250 ha which are referred as L1 and L2 (Fig. 1). The LiDAR sensor was operated at a frequency of 50 kHz and flown at a height of about 2000 m with a laser spot spacing of 1.12 m (Asner et al. 2007). The LiDAR data were collected in April 2008.

3.2 Precipitation data

Moisture condition is one of the most important factors influencing the radar backscatter. Increasing surface moisture resulting from rainfall, fog or dew, affects the dielectric constant of ground targets, which accordingly increases the backscatter (Leckie and Ranson 1996). In order to identify possible influence of moisture on the SAR data, the sum of precipitation during four days prior the acquisition date (including the acquisition day) for each PALSAR scene was calculated (Table 1). The precipitation data used were recorded from four weather stations (Fig. 1), located in the KNP within the PALSAR footprints, with daily resolution for the period between 1st of January 2007 and 30th of September 2010. The precipitation data were made available by the South African National Parks

(SANParks 2013a, b). No precipitation events were recorded at any of the weather stations on any of the acquisition dates. Interestingly no record of precipitation were observed prior to any acquisition dates at the weather stations Tshokwane (TSH) and Talamati (TAL), while some were recorded at the weather stations Skukuza (SKZ) and Nhlanguleni (NHL). This illustrates the rainfall gradients mentioned previously and the high rainfall spatial heterogeneity in the region. The precipitation data shows expected rainfall patterns for the various seasons, i.e. DRY: smallest and less frequent rainfall event; MWET: high and most frequent rainfall event; EWET: most variable season.

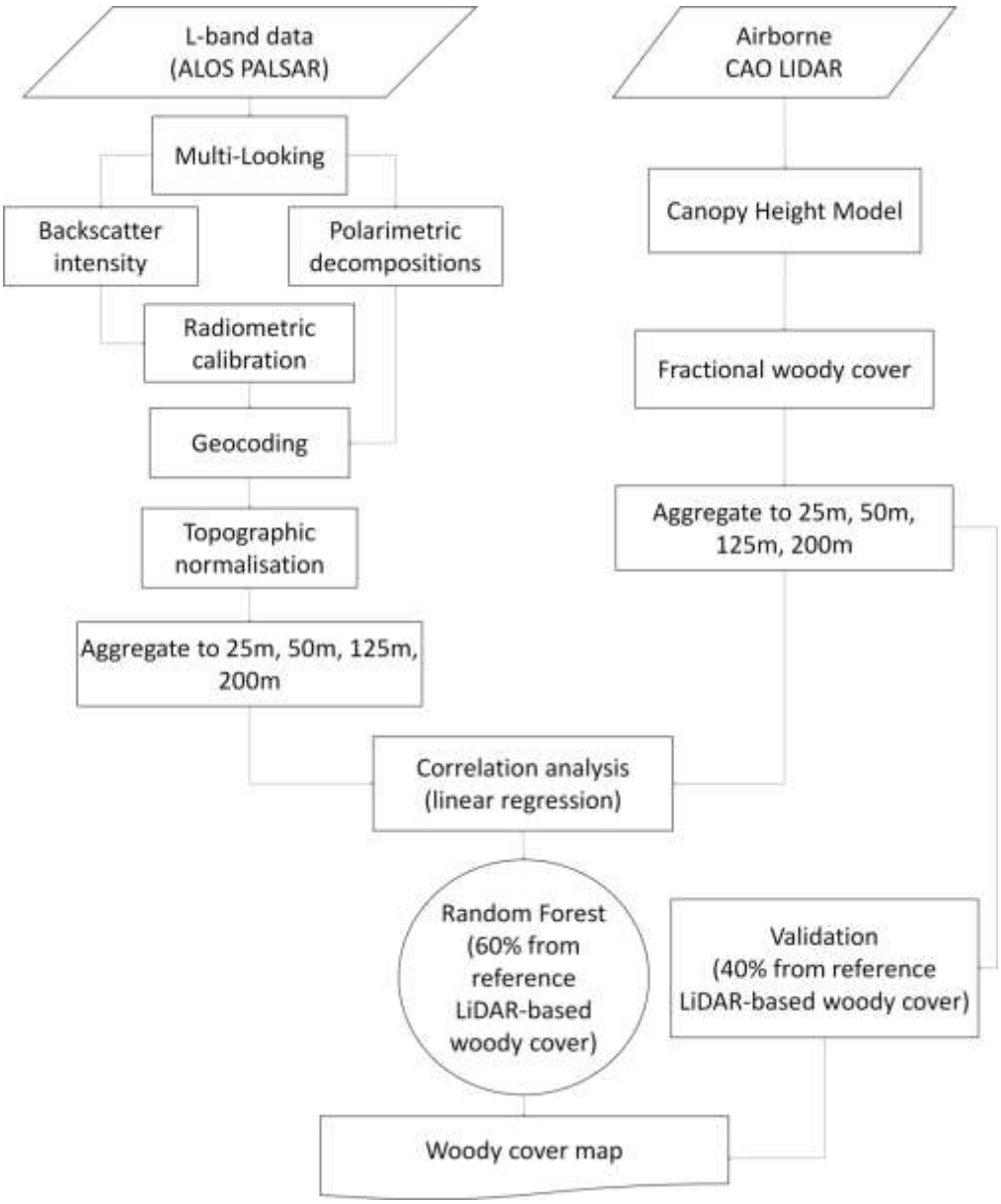

Figure 2: Flow chart of the data processing and analysis steps

3.3 Processing steps

From the SLC (Single Look Complex) data multi-looked backscatter values and two polarimetric decompositions were calculated (Fig. 2). A fractional woody cover metric was derived from the high resolution LiDAR dataset, which served as calibration and validation of the SAR models. The relationships between SAR and LiDAR datasets were analyzed at different spatial resolutions. The SAR modes were processed with different multi-looking factors and the LiDAR woody cover values were aggregated at the corresponding spatial resolution. A simple linear regression was built between

the SAR parameters and LiDAR-based woody cover metric to analyze the effects of the spatial resolution and seasonality. A SAR-based woody cover map was modeled at the optimal spatial resolution using the best seasonal images and a machine learning algorithm "Random Forests" (RF) (Breiman 2001). Finally validation of the derived products was conducted using coefficient of determination (R^2), root mean square error (RMSE), relative RMSE (rRMSE), and estimation bias.

3.3.1 SAR data processing

A multi-look technique was first applied on the SLC level 1.1 datasets. The multi-look factors used for the different acquisition modes are shown in Table 2. The multi-look images were radiometrically calibrated using a sensor-specific calibration factor (-115 dB). A coherence matrix [T] using 1 and 7 looks in range and azimuth directions, respectively, was firstly estimated for the two full polarimetric images. Then from the coherence matrices model-based polarimetric decompositions of Freeman-

Table 2: Multi-look factors applied to the ALOS PALSAR images used in this study

Mode	Pixel size (original, radar geometry) Rg x Az [m]	Pixel size (after multi-looking, radar geometry) Rg x Az [m]	Pixel size (map geometry) Rg x Az [m]	Processing steps
PLR	9.37 x 3.59	9.37 x 25.13	25 x 25	1 look rg x 7 look az
FBD	9.37 x 3.23	9.37 x 16.15	12.5 x 12.5	1 look rg x 5 look az
FBS	4.68 x 3.23	4.68 x 6.46	6.25 x 6.25	1 look rg x 2 look az

FBS Fine Beam Single Polarization mode; FBD Fine Beam Dual Polarization mode; PLR Polarimetry mode; Rg range direction; Az azimuth direction.

Durden (Freeman and Durden 1998) and Van Zyl (van Zyl 1989) were derived using a moving window of 5x5 pixels. The SAR images (backscatter intensities and polarimetric decomposition components) were then geocoded using a 20 m digital elevation model (DEM). The main steps of the geocoding procedure are: (i) generation of look-up table with position information of each pixel in SAR range-Doppler and DEM map geometry, (ii) generation of simulated SAR intensity image from DEM in a map geometry and transformation to SAR geometry, (iii) co-registration of simulated with real SAR intensity image in SAR geometry, (iv) look-up table refinement and (v) transformation of SAR range-Doppler to a map geometry (GAMMA 2008). The geocoding accuracy of the terrain corrected products were on average for all SAR products 12.3 m ± 11.4 m and 10.2 m ± 7.5 m in range and azimuth directions, respectively.

In the next step the geocoded SAR parameters were normalized for topographic effects according to Castel et al. (2001) and Stussi et al. (1995) (Eq. 1). The topography corrected backscatter coefficients (σ^0_{cor}) were calculated using the linear backscattering coefficient (σ^0), the true ground scattering area (A_{slope}), the ground scattering area for theoretically flat terrain (A_{flat}), as well as the incidence angle for flat terrain (θ_{ref}) and the actual local incidence angle (θ_{loc}) (Castel et al. 2001; Stussi et al. 1995):

$$\sigma^0_{cor} = \sigma^0 \frac{A_{flat}}{A_{slope}} \left(\frac{cos\theta_{ref}}{cos\theta_{loc}} \right)^n \quad (1)$$

The parameter *n* allows for an adaption of the angular adjustment according to the prevalent land cover and scattering processes. In this study, n was set to 1.

The geocoded and terrain corrected SAR parameters with different pixel sizes were aggregated to specific spatial resolutions (25 m, 50 m, 125 m and 200 m) using a block averaging technique, e.g. to aggregate to 50 m spatial resolution a mean value was calculated by combining 16 pixels (4x4) for FBD data. The aggregation was done to analyze the influence of scale on the SAR and LiDAR woody cover relationships and to determine an optimal resolution for woody cover mapping. The aggregation of pixels reduces the influence of speckle noise in the SAR data and of the co-registration uncertainty

between LiDAR and SAR data (Saatchi et al. 2011). In order to evaluate the amplitude of speckle noise in the SAR data an equivalent number of looks (ENL) can be calculated using two approaches. Oliver and Quegan (2004) determined ENL over homogeneous areas by dividing the mean square backscatter intensity by variance (e.g., ENL=mean²/variance). Since South African savannas represent very heterogeneous areas, it is challenging to find a set of homogeneous areas over 4 ha (for data at 200 m spatial resolution). Therefore, we preferred to estimate ENL using a theoretical approach (as opposed to a data-driven estimate) based on the nominal number of looks and signal to noise ratio (SNR) according to ESA (2007), and equation (2):

$$ENL = \frac{N_r * N_{az}}{\left(1 + \frac{1}{SNR}\right)^2} \quad (2)$$

where N_r and N_{az} are the number of range and azimuth looks, respectively. An increase in the ENL with spatial aggregation indicates a reduction of speckle noise in the multi-looked SAR data (Table 3).

Table 3: Equivalent number of looks (ENL) at different spatial resolutions. ENLs represent a mean value for HH and HV polarizations for FBD data and a mean value for HH, HV, VH and VV polarizations for PLR data

	ENL_25m	ENL_50m	ENL_125m	ENL_200m
FBS_03feb07	27.50	112.86	688.37	1580.77
FBS_08feb09	27.30	111.08	693.65	1623.14
FBS_27dec09	27.14	113.06	701.46	1593.24
FBS_11feb10	27.58	112.24	694.14	1625.41
FBD_06aug07	17.16	70.46	431.51	1025.32
FBD_23sep08	17.06	69.97	425.79	1101.48
FBD_11aug09	17.19	70.07	422.62	1065.63
FBD_29sep10	17.12	69.86	428.40	1005.06
PLR_14apr07	5.51	22.84	148.20	372.76
PLR_19apr09	5.47	22.35	143.19	362.63

H horizontal polarization; V vertical polarization; FBS Fine Beam Single Polarization mode; FBD Fine Beam Dual Polarization mode; PLR Polarimetry mode

Multi-looking, radiometric calibration, geocoding as well as topographic normalization of all SAR parameters was done using GAMMA software (http://gamma-rs.ch). The calculation of polarimetric

decompositions was performed in PolSARPro 4.2.0. In total, 20 backscattering intensities in HH, HV, VH and VV polarizations corresponding to ten FBS, FBD and PLR PALSAR images and two polarimetric decompositions were analyzed (Table 1).

3.3.2 Estimates of woody cover using LiDAR data

From the raw discrete-return LiDAR point cloud data physical models of ground surfaces (DEM) and top-of-canopy surface models (CSM) were generated using the REALM (Optech Inc., Vaughn, Canada) and Terrascan/Terramatch (Terrasolid Ltd., Jyväskylä, Finland) software packages. A Canopy Height Model (CHM) was derived by subtracting the DEM from the CSM. During the acquisition of the LiDAR data, a concurrent field campaign was undertaken to validate the height information obtained. The heights of 883 trees and shrubs were measured using a graduated pole and a hypsometer and compared to the LiDAR-based woody plant height (R^2=0.93, $p<0.001$, standard error=0.73 m) (Wessels et al. 2011). The correlation between the field-based and LiDAR-based heights was high. However, a number of woody plants below 2 m were not detected in the LiDAR CHM mainly due to i) the limited target cross section within 1.12 m pixels, ii) the user-defined thresholds for identifying ground returns and iii) the LiDAR reset time (ca. 0.71 m). The 1.12 m pixel size CHM was classified into woody and non-woody classes using a threshold of 1 m above ground. The threshold was considered a good trade-off between capturing the smallest woody plants (i.e. shrubs) and excluding tall herbaceous plants (Wessels et al. 2011). The percentage woody cover was calculated for a pixel size of 5x5 m and was aggregated to the same spatial resolutions (25 m, 50 m, 125 m and 200 m) generated with the SAR data. The aggregation of LiDAR-based woody cover was carried out by calculating a mean value of aggregated pixels.

3.4 Relationships between SAR parameters and LiDAR-based woody cover

In order to identify the most correlated SAR data to the LiDAR-derived woody cover data, for each SAR parameter a simple linear regression (Eq. 3) was applied at all investigated resolutions:

$$\sigma^0 = a * W + b \quad (3)$$

where σ^0corresponds to the backscatter (in db scale) and W represents the woody cover (%).

After the analysis of the relationships between the woody cover and SAR data, an optimal spatial resolution was determined for mapping the woody cover, representing a trade-off between the efficiency of the model (as assessed with R^2) and the spatial details.

3.5 Estimates of woody cover from SAR data

The SAR-based models developed for predicting woody cover used the Random Forests (RF) algorithm (Breiman 2001), and were calibrated with the LiDAR-based woody cover maps. The RF by Breiman (2001) is a machine learning method and builds on the Classification And Regression Trees (CART) algorithm (Breiman et al. 1984). In contrast to CART many regression trees are generated in RF instead of one, which generally produce more accurate results (Avitabile et al. 2012). The trees are grown with a random selection of predictors at each node as well as with a random subset of samples for each tree with the aim of avoiding overfitting. In order to calculate a single estimate, the predictions of each regression tree are averaged (Breiman 2001). The RF is a computational efficient and robust non-parametric model and was successfully applied to map vegetation structure metrics (e.g., AGB, tree height) with high retrieval accuracy at large spatial scales (e.g., Avitabile et al. 2012; Baccini et al. 2008; Cartus et al. 2012). Our random forests were generated with 500 regression trees. To avoid autocorrelation we modeled woody cover using LiDAR and SAR samples placed at a distance of 50 m from each other. This was selected following analysis of semi-variogram on tree height, where Wessels et al. (2011) using the same dataset found that samples taken 50 m apart, or further, could be treated as independent (Beale et al. 2010). Then, randomly 60% of the LiDAR data were selected for model calibration and the remaining 40% were used for validation.

We modeled woody cover using three scenarios: (1) a single date scenario (i.e., woody cover map based on a single SAR image), (2) a multi-seasonal scenario (i.e., woody cover map based on SAR

images from the same year and different seasons, based on key phenological difference), and (3) a multi-annual scenario (i.e., woody cover map based on SAR data from different years). For the single date models the SAR images with the strongest correlations were selected. The multi-seasonal model was applied only on the SAR data from the year with the greatest number of date available (2009). Finally, for the multi-annual model the eight datasets with the strongest correlations spanning over the four years were selected for the modeling and mapping of woody cover estimates. A linear regression between observed and predicted woody cover was calculated and the model performance was assessed with the coefficient of determination (R^2), root mean square error (RMSE), relative RMSE (rRMSE), and estimation bias.

Furthermore, as a spatially explicit reference dataset was available (LiDAR CHM), we tested how the number of samples used impact on the model prediction performance. For this, we applied a stratified sampling from the L1/L2 LiDAR data. We divided firstly the LiDAR data in three classes: sparse woody cover (<20%), moderately dense woody cover (20-50%) and dense woody cover (>50%). Then we extracted from each class 5, 10, 20, 30, 60, 90, 120, 150 and 180 samples, which resulted in a total number of samples of 15, 30, 60, 90, 180, 270, 360, 450 and 540. Using these samples we calibrated the RF models with the eight backscatters from the four FBD images acquired during the dry season. After the model calibration we validated the RF models with another independent equivalent number of samples (i.e. between 15 and 540 samples). We ran the RF model 100 times for each number of samples, i.e., we selected calibration/validation data 100 times. Furthermore, we used all LiDAR samples for calibration and validation. For this, we extracted randomly 60% (6468 samples) and 40% (4312 samples) calibration/validation data 100 times.

4. Results and discussion

4.1 Relationships between SAR parameters and LiDAR-based woody cover map

ALOS PALSAR datasets comprising various modes and polarizations (HH, HV, VH, VV), seasons (DRY season, MWET season and EWET season), as well as two polarimetric decompositions (by

Table 4: Coefficients of determination (R^2) between SAR parameters and LiDAR derived woody cover at different spatial resolutions and for three seasons

		25 m	50 m	125 m	200 m
DRY	FBD_HH_06aug07	0.3164	0.5915	0.6658	0.7130
	FBD_HH_23sep08	0.2233	0.5787	0.6141	0.6348
	FBD_HH_11aug09	0.2822	0.5993	0.6664	0.7104
	FBD_HH_29sep10	0.2893	0.4985	0.6122	0.6762
	FBD_HV_06aug07	0.3521	0.6184	0.6868	0.7250
	FBD_HV_23sep08	0.2458	0.5909	0.6087	0.6181
	FBD_HV_11aug09	0.3088	0.6197	0.6749	0.7159
	FBD_HV_29sep10	0.3088	0.5111	0.6086	0.6649
MWET	FBS_HH_03feb07	0.2940	0.3437	0.4825	0.7095
	FBS_HH_08feb09	0.3241	0.3162	0.5241	0.4839
	FBS_HH_27dec09	0.1229	0.1874	0.5768	0.3720
	FBS_HH_11feb10	0.2347	0.2803	0.3947	0.4652
EWET	PLR_HH_14apr07	0.0447	0.1551	0.2620	0.2974
	PLR_HH_19apr09	0.0757	0.2579	0.4510	0.5959
	PLR_VV_14apr07	0.0229	0.0861	0.1608	0.1913
	PLR_VV_19apr09	0.0577	0.2101	0.3826	0.5102
	PLR_HV_14apr07	0.0922	0.2759	0.4381	0.5099
	PLR_HV_19apr09	0.1200	0.3465	0.5362	0.6784
	PLR_VH_14apr07	0.0871	0.2629	0.4220	0.4888
	PLR_VH_19apr09	0.1169	0.3380	0.5272	0.6688
EWET	Freeman_Vol_14apr07	0.1661	0.3512	0.4554	0.5190
	Freeman_Vol_19apr09	0.1992	0.4157	0.5448	0.6700
	VanZyl_Vol_14apr07	0.1647	0.3484	0.4525	0.5162
	VanZyl_Vol_19apr09	0.1997	0.4159	0.5447	0.6689

DRY dry season; EWET end of wet season; MWET middle of wet season; H horizontal polarization; V vertical polarization; FBS Fine Beam Single Polarization mode; FBD Fine Beam Dual Polarization mode; PLR Polarimetry mode; Vol volume component. Cell are shaded with grey tones ranging from white to black corresponding to an increasing R^2 ($R^2 \leq 0.5$ white, $0.5 < R^2 \leq 0.6$ light grey, $0.6 < R^2 \leq 0.7$ medium grey, $R^2 > 0.7$ black), in bold mean values

Freeman and Durden 1998; van Zyl 1989) were investigated and compared with LiDAR-derived woody cover reference data at various spatial resolutions (Table 4).

4.1.1 Influence of seasonality

The analyzed SAR data were acquired during three seasons (DRY, MWET and EWET), so that it was possible to determine the optimal season for mapping of woody cover in southern African savannas. Datasets in the HH polarization from the three respective seasons were compared with the LiDAR data, as this was the only polarization available for all investigated seasons (Fig. 3).

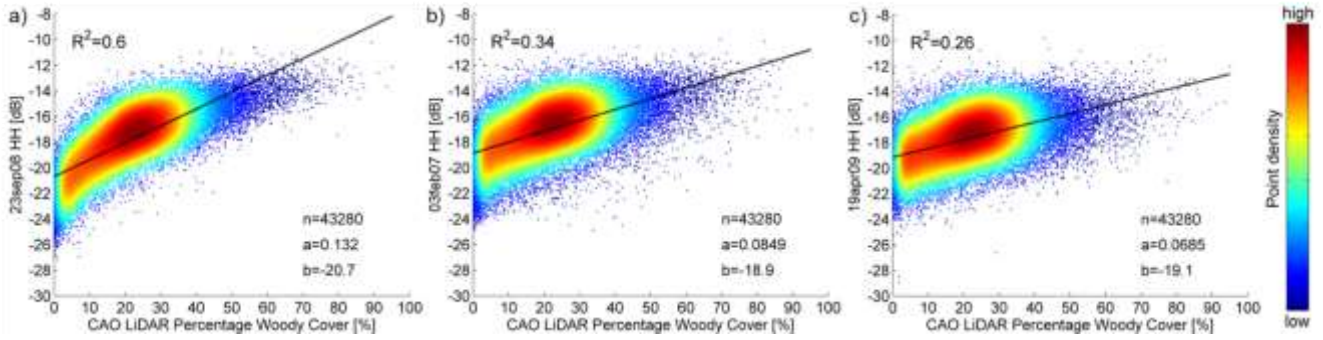

Figure 3: PALSAR HH backscatter intensities from a) 23.09.08 (DRY: dry season), b) 03.02.07 (MWET: middle of wet season) and c) 19.04.09 (EWET: end of wet season) plotted against LiDAR-based woody cover at 50 m spatial resolution

The highest correlations with the woody cover were observed from the DRY datasets (August-September). During this time the grass layer is completely dry and most of the deciduous trees (mostly occurring in this landscape) are devoid of leaves, allowing the radar signal to fully penetrate the canopy and interact only with the woody parts. The higher and variable moisture level in the landscape in summer and autumn may have led to a larger spread of points around the regression line in the MWET and EWET data compared to the DRY data (Fig. 3). In the region most precipitation occurs in the form of short duration and high intensity thunderstorms (convective process), which lead to variable precipitation over relatively short distance. During the dry season there is almost no rainfall (Table 1), thus the soil moisture content is at its minimum resulting in a low mean backscatter (-22 dB) from bare surface, i.e. surface with 0% woody cover, and a high dynamic range of the backscatter. For MWET and EWET data (Fig. 3), the mean backscatter from bare surface is higher (-20 dB) and the

dynamic range of the backscatter is reduced compared to dry conditions. Furthermore, it was observed that the datasets from the MWET season (January-February) show a stronger correlation to the woody cover compared to the data from the EWET season (April-May) (Table 4, Fig. 3). This may be caused by a more homogeneous distribution of water in the landscape in the middle of the rainy season compared to the end of the rainy season. Most precipitations occur between December and March, with a peak in January-February corresponding to the period of highest vegetation productivity. Rainfall drops between April and May which is a period of transition during which the drying processes begin with different effects along catena and geological types (granite versus gabbro), resulting in an increase in the variability of moisture in the landscape (Venter et al. 2003). Following a time delay the annual senescence process starts, first with the grasses which are more directly dependent on moisture availability in the top soil, then with woody plants through yellowing and leaf shedding. This process been closely linked to water availability, and also to a lesser extent to species-specific phenology (e.g. species such as *Acacia nigrescens* shed their leaves early compared to other species (Cho et al. 2012)), induces further variability in the landscape with the gradual change from a dominance of green - leaf-on patches to the dominance of non-green - leaf-off patches toward the dry season. Similar seasonal patterns were observed with RADARSAT-2 C-band data in the same region (Mathieu et al. 2013).

Finally, we compared the backscatter intensities of each SAR image to the reference image acquired on the 23rd September 2008 (Fig. 4). The image was selected as reference because it was the only image acquired during the dry season and the same year of the LiDAR acquisition. We compared HH polarizations only, as MWET data were acquired in single polarization mode. The colors showed in Fig. 4 correspond to three classes of woody cover as measured by the LiDAR data: sparse woody cover (<20%, code s, yellow), moderately dense woody cover (20-50%, code md, green), and dense woody cover (>50%, code d, blue). Overall, when compared to the data from the dry season, the backscatters are consistent, well aligned the 1:1 line and with a reduced variability compared to EWET and MWET. This indicates high backscatter stability over the years, and suggests that modeling of

woody cover would be more robust using dry season data. Important positive offsets were observed for the EWET and MWET date, at which significant precipitation (>5 mm) was recorded four days prior

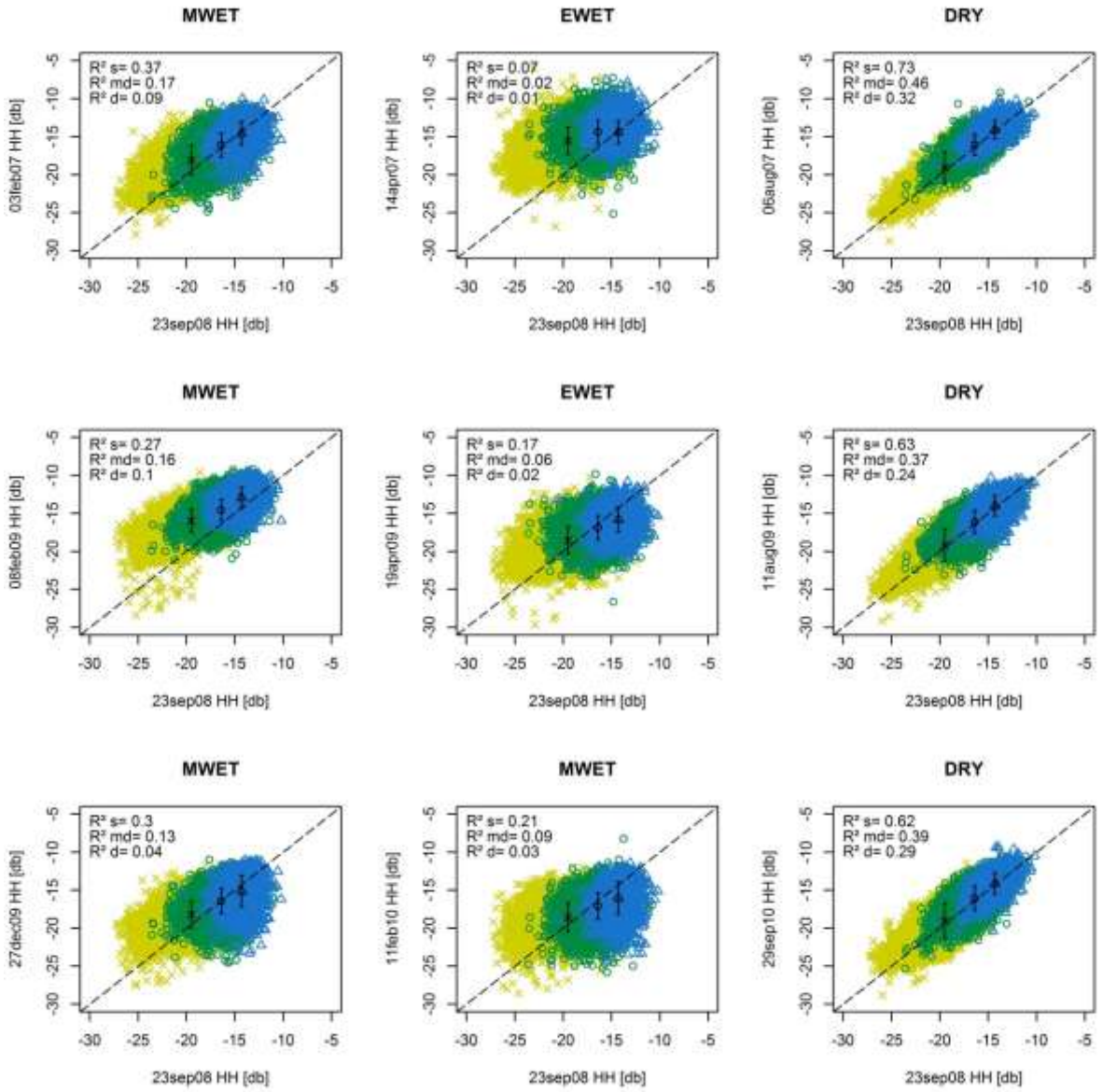

Figure 4: Comparison of HH backscatters of the single SAR images with the reference backscatter image from the dry season 23.09.08. DRY: dry season, MWET: middle of wet season, EWET: end of wet season. The color corresponds to three classes of woody cover as measured by the LiDAR data: sparse woody cover (<20%, s, yellow), moderately dense woody cover (20-50%, md, green), and dense woody cover (>50%, d, blue). Bars indicate a mean value with a corresponding standard deviation per woody cover class, cross for sparse woody cover, circle for moderately dense woody cover, and triangle for dense woody cover.

to the image acquisition (03feb07, 14apr07, and 08feb09). Furthermore, the MWET and EWET data with low woody cover (yellow color) showed the highest positive offsets compared to the reference image. Sparse woody cover inherently presents many gaps through which the microwaves can reach the ground (soil and grasses) and be more affected by a higher soil moisture content compared to the winter season. Correlations for each dataset follow the order DRY>MWET>EWET. This seems to match a logical order of moisture and landscape heterogeneity pattern as mentioned above.

4.1.2 Influence of polarization

Polarization comparisons were only meaningful for images acquired during the same season. Co- (HH) and cross-polarized (HV) datasets from the dry season showed equally strong correlations with the LiDAR reference data (Table 4). Since the woody plants at this time period are mostly devoid of leaves, co- and cross-polarized waves interact primarily with the woody vegetation components (i.e. branches and trunks). In contrast, there is a weaker relationship for the co-polarized datasets (HH, VV) during the EWET season compared to the cross-polarized datasets (HV, VH, Table 4). The woody vegetation at this time period have leaves, resulting in an increase of the volume scattering. The latter is known to better correlate with cross-polarized intensities (Le Toan et al. 1992), and would contribute to improvement of correlations between the cross-polarized datasets and the woody cover. Moreover, the co-polarized datasets, being more sensitive to surface properties compared to cross-polarized datasets (Beaudoin et al. 1994), are likely to be more affected by moisture variability prevalent at the end of the wet season (drying season).

At fine spatial resolutions (25 and 50 m) the volume components of the Freeman-Durden and Van Zyl decompositions show a slightly higher correlation to the LiDAR-based woody cover than the co- and cross-polarized intensities (Table 4). This most likely stems from prior averaging of the backscatter values in polarimetric decompositions, as they were calculated using a moving window approach, which leads to the reduction of speckle noise. The performance of the volume components over the cross-polarized intensities was only marginally improved at coarser spatial resolutions (125 and

200 m) (Table 4). In general the result indicates that the volume components derived from the decomposition do not provide a significant benefit to the mapping of canopy cover compared to single cross-polarized bands. The three-component polarimetric decompositions of Freeman-Durden has been reported to overestimate the total volume scattering power, due to an assignment of all cross-polarized backscattered power to this component (van Zyl et al. 2008). Despite this observation, both the Freeman-Durden and Van Zyl volume components produced very similar results. In order to reduce the Freeman-Durden overestimation, some authors (e.g., Singh et al. 2013; Yamaguchi et al. 2005; Yamaguchi et al. 2011) suggested to introduce a fourth scattering component (helix scattering). However, the implementation of this fourth scattering component was found to be more relevant for describing artificial targets (Yamaguchi et al. 2005) and less effective in vegetated-dominated areas (Antropov et al. 2011). Other researchers (e.g., Antropov et al. 2011; Wentao et al. 2010) proposed alternative decomposition models, which implement a more accurate description of the volume component. Further investigation of L-band dry season polarimetric data (as overall in this season, SAR data showed the highest correlation to woody cover) with alternative polarimetric decomposition models (e.g., Antropov et al. 2011; Singh et al. 2013) should be encouraged. Since polarimetric decompositions did not provide significant benefits over single polarized bands, they were not used for the woody cover modeling.

4.1.3 Impact of spatial aggregating

The relationships between SAR data and LiDAR-based woody cover varied as a function of the spatial resolution or scale at which the analysis was performed. Fig. 5 shows the relationships between the HV backscatter from the 23rd of September 2008 and the LiDAR woody cover at four different resolutions (25 m, 50 m, 125 m and 200 m). The averaging of pixels minimized the influence of speckle, co-registration uncertainties, errors in the reference data, as well as the effect of landscape heterogeneity, leading to the reduction in the spread of points and an increase in the correlation between the two datasets (Saatchi et al. 2011). Similar trends were observed for all seasons (Table 4). A sharp increase in the significance of the relationship between the DRY SAR dataset and the LiDAR dataset was

detected at a spatial resolution of 50 m, after which the R^2 improved at a lesser rate for increasing scales of aggregation. 50 m was selected as a good trade-off between the smallest possible mapping unit and the achievable accuracy.

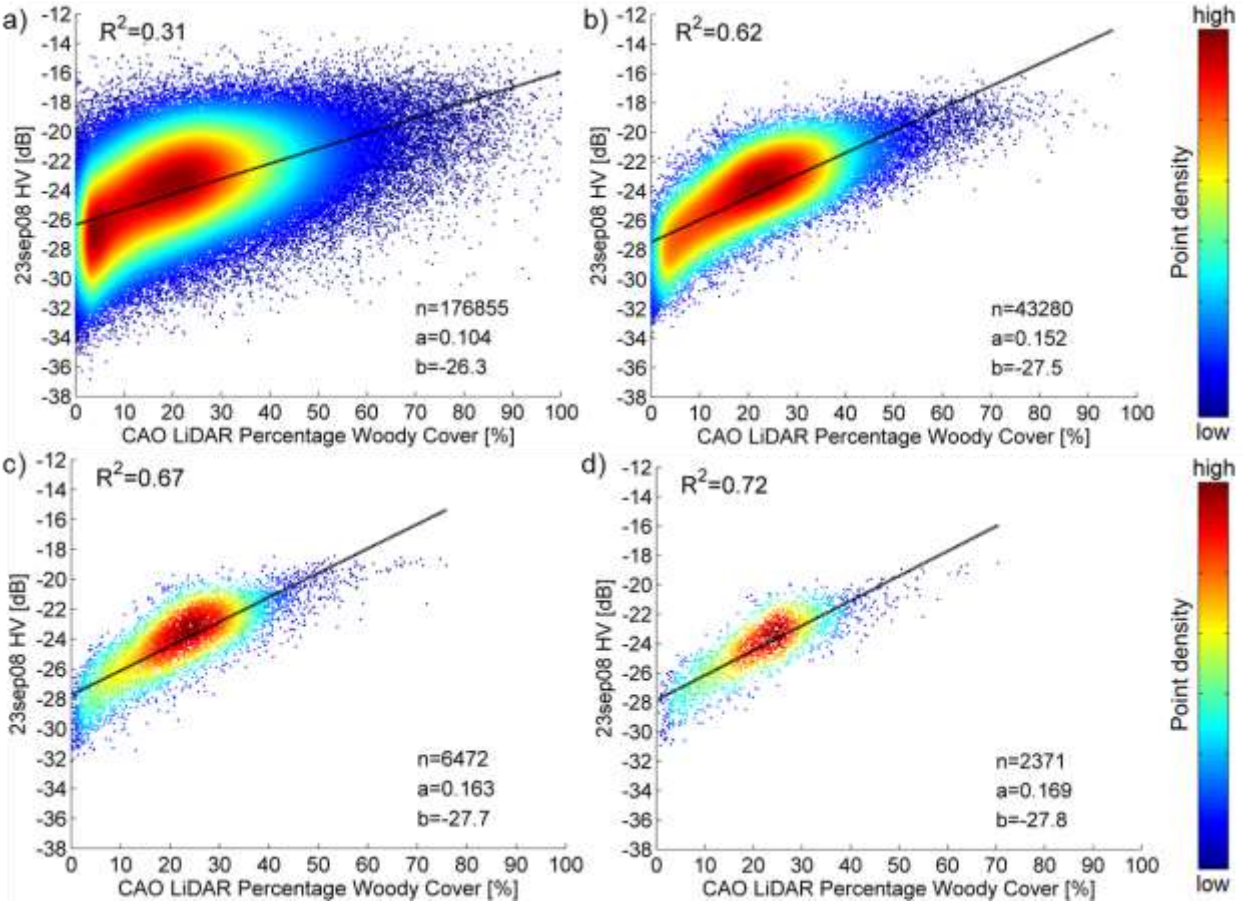

Figure 5: PALSAR HV backscatter intensity from 23.09.08 (DRY: dry season) at a) 25 m, b) 50 m, c) 125 m and d) 200 m spatial resolution plotted against LiDAR-based woody cover (n from 176855 to 2371)

4.2 Woody cover modeling and mapping

4.2.1 Model assessment and map validation

Based on the results presented in section 4.1, we selected three woody cover modeling scenarios, using SAR images acquired at a single date, during multiple seasons of the same year, or over the multiple years. For all three scenarios woody cover was modeled at a spatial resolution of 50 m. The single date scenario produced four models based on the HH and HV SAR backscatters from the dry season for the year 2007, 2008, 2009, and 2010 individually (Table 5). For the multi-seasonal model we selected four

Table 5: Retrieval errors for woody cover estimates based on three scenarios: single date (2007, 2008, 2009, and 2010 individually), multiple season for a single year (2009 only, as this year with the greatest number of date available), and multiple years imagery (from 2007 to 2010)

	R^2	RMSE (%)	rRMSE (%)	Bias
Single year DRY PALSAR (FBD_HH_06aug07, FBD_HV_06aug07)	0.64	8.67	9.12	0.46
Single DRY PALSAR (FBD_HH_23sep08, FBD_HV_23sep08)	0.66	8.45	8.89	0.44
Single DRY PALSAR (FBD_HH_11aug09, FBD_HV_11aug09)	0.62	8.97	9.43	0.86
Single DRY PALSAR (FBD_HH_29sep10, FBD_HV_29sep10)	0.52	10.14	10.66	1.01
Multi-seasonal DRY-MWET PALSAR (FBS_HH_08feb09, FBS_HH_27dec09, FBD_HH_11aug09, FBD_HV_11aug09)	0.64	8.72	9.17	0.94
Multi-annual PALSAR (FBD_HH_06aug07, FBD_HV_06aug07, FBD_HH_23sep08, FBD_HV_23sep08, FBD_HH_11aug09, FBD_HV_11aug09, FBD_HH_29sep10, FBD_HV_29sep10)	0.71	7.88	8.29	0.9

R^2 coefficient of determination; RMSE root mean square error; DRY dry season; MWET middle of wet season

co- and cross-polarized SAR backscatter from 2009 (as this year had the highest number of date available) from two seasons DRY and MWET (note: PLR data from EWET were not used, as they cover a smaller area) (Table 5). For the multi-year model, eight co- and cross-polarized L-band backscatter intensity images from the dry season of 2007 to 2010 were used as predictor of the woody cover (Table 5). Regarding the single data models, the highest performance (R^2=0.66, RMSE=8.45%) was observed with the DRY SAR image from 2008, corresponding to the same year as the LiDAR dataset. Performance decreased as the time difference between the SAR and LiDAR datasets increased, especially in 2010 which marks the largest time difference. The 2009 multi-seasonal model (MWET and DRY) produced a slightly higher performance than the 2009 single date DRY model (R^2=0.64, RMSE=8.72% vs. R^2=0.62, RMSE=8.97%) (Table 5). The best results (R^2=0.71, RMSE=7.88%) were obtained for the multi-annual model. The results indicate that woody cover retrieval is possible with a reasonable accuracy using single PALSAR scene from the dry season. However, single dates can be affected by variability related to environmental conditions (e.g., soil moisture) or disturbances (e.g.,

fire). These can be reduced by using multi- to hyper-temporal datasets (Main et al. 2014; Santoro et al. 2011), and here models were improved using a time series of scenes acquired during winter over multiple years despite the possibility of woody cover change between years, for instance changes of cover induced by large herbivores such as elephants (Asner and Levick 2012). Another source of uncertainty in the model is related to the timing of the acquisition of the LiDAR data. The LiDAR campaign was undertaken during the start of wet-dry transition season (April) after a relatively dry late summer. By far most tree canopies were still green and with leaves. However, this may have introduced some noise in the LiDAR woody cover maps, since the variability of water availability

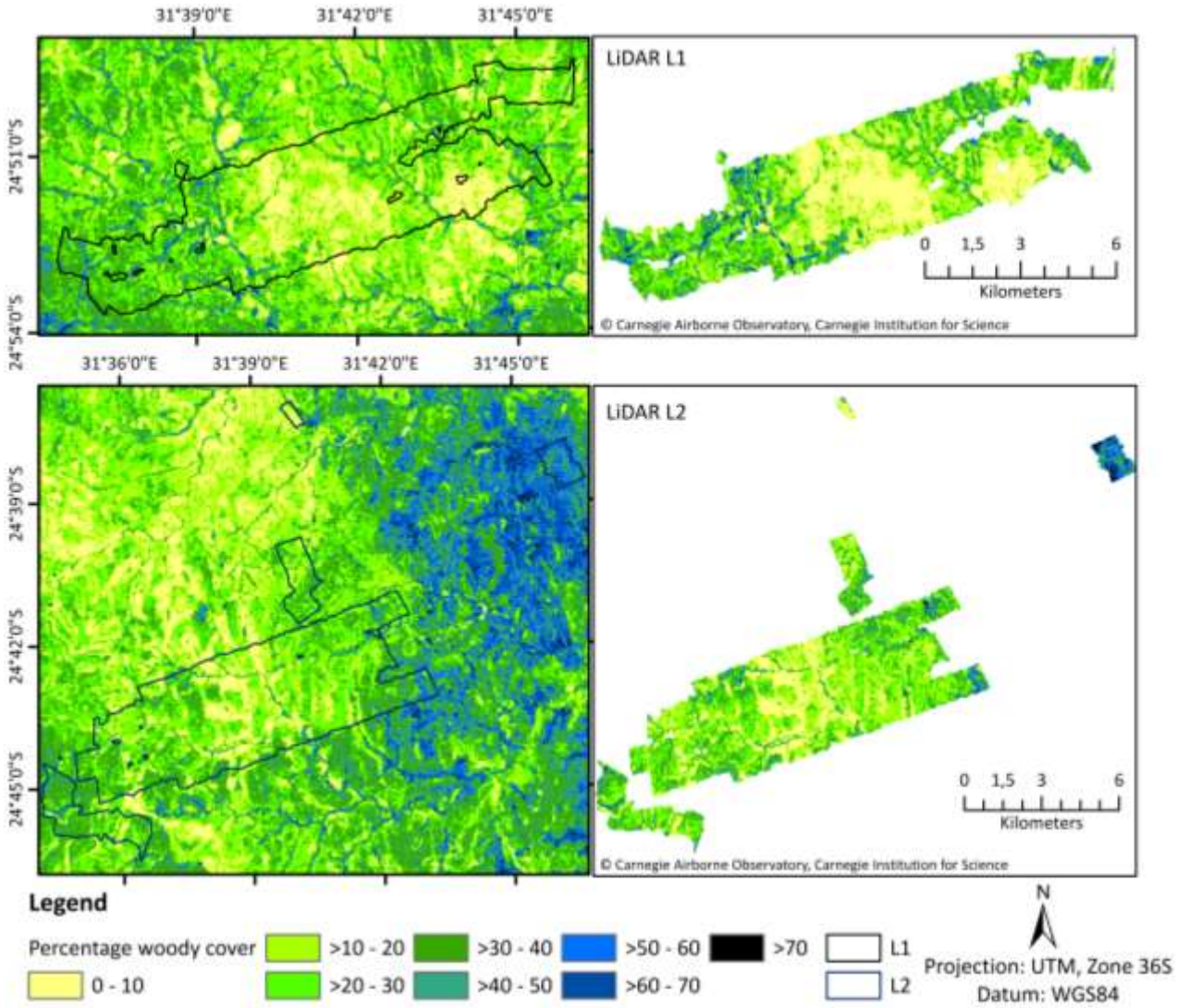

Figure 6: Comparison between the PALSAR-based woody cover map (left) and CAO LiDAR-based woody cover map (right) for the test sites L1 and L2. The PALSAR-based woody cover map was produced with a random forest algorithm, at a spatial resolution of 50 m, and from dry season images, HH and HV polarization, acquired in 2007, 2008, 2009 and 2010.

fire). These can be reduced by using multi- to hyper-temporal datasets (Main et al. 2014; Santoro et al. 2011), and here models were improved using a time series of scenes acquired during winter over multiple years despite the possibility of woody cover change between years, for instance changes of cover induced by large herbivores such as elephants (Asner and Levick 2012). Another source of uncertainty in the model is related to the timing of the acquisition of the LiDAR data. The LiDAR campaign was undertaken during the start of wet-dry transition season (April) after a relatively dry late summer. By far most tree canopies were still green and with leaves. However, this may have introduced some noise in the LiDAR woody cover maps, since the variability of water availability across the landscape and species-specific phenology would lead to patches with variable senescence stages, resulting in a possible overall underestimation of the real woody cover.

The visual comparison of the multi-annual SAR-based woody cover map (Fig. 6 left) with the LiDAR reference data (Fig. 6 right) shows a high degree of agreement. For instance, patterns of vegetation along the rivers (riparian forests) or the large bare patterns in the central section of L1 and L2 match

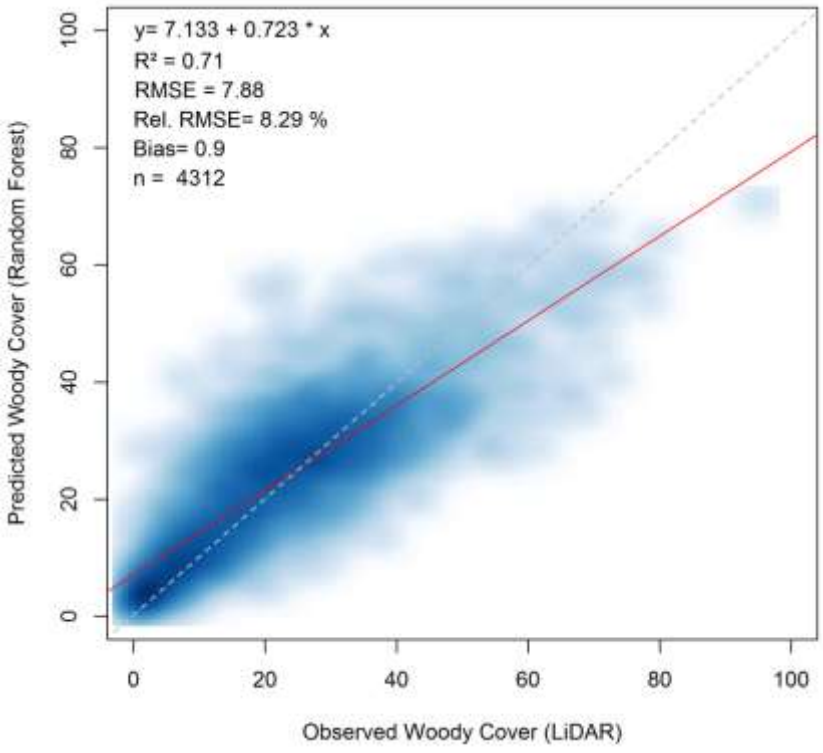

Figure 7: SAR-based prediction of woody cover plotted against LiDAR-based observed woody cover. Red line is the regression line, and dotted line is the 1:1 line.

well the distribution of woody vegetation in the LiDAR data. The linear regression between the predicted SAR-derived woody cover values and the LiDAR-based woody cover observations for the multi-annual model is shown in Fig. 7 (R^2=0.71, RMSE=7.88%, rRMSE=8.29% and bias=0.9). The low bias value points to a low difference between the modeled and measured values. However, the deviation of the linear regression from the 1:1 relationship indicates an overestimation of the prediction in the areas sparsely vegetated and an underestimation in the areas densely vegetated. This is also evident in the estimated bias calculated per class of woody cover (Table 6). In terms of R^2 the

Table 6: Retrieval errors for sparse, moderately dense and dense woody cover estimates based on the multi-annual SAR scenario

	R^2	RMSE (%)	rRMSE (%)	Estimated Bias	N
Sparse woody cover (<20%)	0.53	7.04	35.18	3.93	2020
Moderately dense woody cover (20-50%)	0.24	7.81	26.05	-0.94	2117
Dense woody cover (>50%)	0.21	14.74	32.71	-11.44	180

R^2 coefficient of determination; RMSE root mean square error

value for sparse wooded areas (<20% woody cover) was more than twice as high as for moderately dense (20-50% woody cover) and dense (>50%) wooded areas, showing a low variation at low woody cover with increasing spread of points at moderately dense and dense woody cover intervals. However, RMSE values at low and moderately dense woody cover were the lowest and similar, while estimated bias for moderately dense woody cover was the lowest. As the sensitivity of SAR signal in dense woody areas decreases (Fig. 3a), the highest uncertainties were produced for this woody cover interval. Despite that at low woody cover the SAR backscatter is mostly affected by surface scattering, sparsely wooded areas were mapped relatively accurately. Moderately dense vegetated areas showed a low R^2 mostly due to a large spread of points, while the rRMSE and the estimated bias for this interval are the lowest compared to the other woody cover ranges. These statistical metrics show under-/-overestimation patterns which are typical for regression tree-based models, as the predictions

of such tree-based models are computed as the average values of the regression trees within each node (Baccini et al. 2008). Mapping accuracy was similar to that reported in Mathieu et al. (2013) and Bucini et al. (2010), with R^2 of about 0.7 and RMSE of about 8%. However, the ALOS PALSAR data were used to produce maps with a higher level of spatial details at 50 m, vs. 90 m for Bucini et al. (2010) and 105 m for Mathieu et al. (2013).

4.2.2 Impact of number of samples on model prediction performance

The impact of number of samples on the model prediction performance is expressed in the statistical metrics of the prediction accuracy and showed in Fig. 8. The mean R^2 values for the different number of samples used were relatively similar (Fig. 8). However, the greater the number of samples was, the smaller the variability of the R^2 value. With an increasing number of samples the mean RMSE and rRMSE decreased as well as their corresponding variability. The variations of estimated bias also decreased with an increasing number of samples. The RF models using a small number of samples (e.g., 15 or 30) can achieve high prediction accuracy; however, the performance of these models is more variable compared to those based on a higher number of samples. Overall, for all statistical metrics the mean stabilizes and the variability is minimum at 180 samples and beyond (or 360 if considering the number of samples required for calibration and validation of the models). Furthermore, Figure 8 also shows the statistic results based on the complete LiDAR dataset. Using all LiDAR samples with a random sampling RMSE, rRMSE, bias and their variability still decreased significantly. In comparison, most of the published studies which have estimated AGB with remote sensing data used less than 100 field samples, with a significant number of those using only 30 to 50 field samples (Fassnacht et al. 2014). This number is typical for researchers based on field sampling, and are generally explained by the costs and sometimes logistical complexities involved in acquiring large sample. Here we show that airborne LiDAR data provide a good alternative to address these limitations, and increase the stability and robustness of prediction performance.

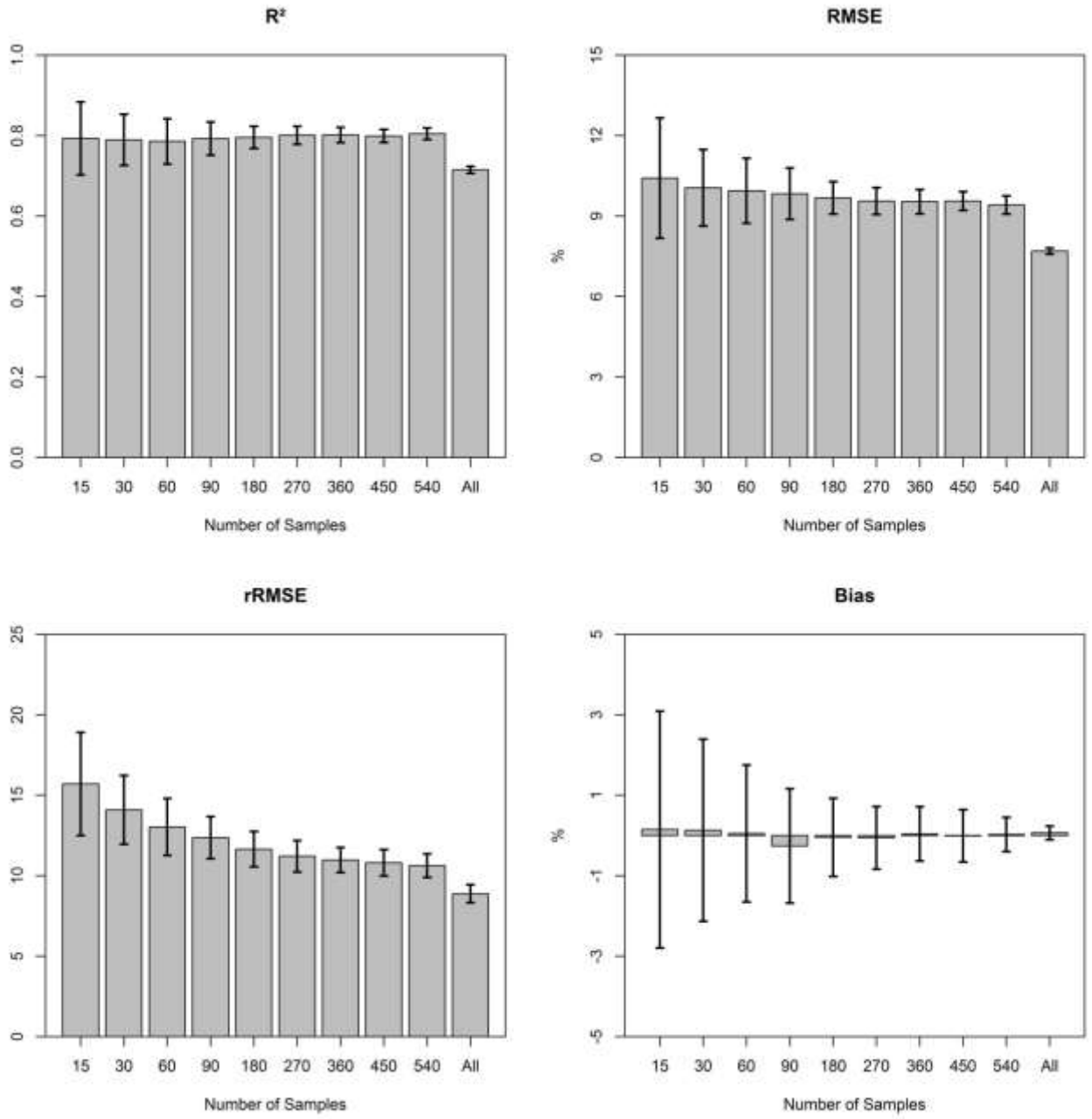

Figure 8: Impact of the number of LiDAR samples used on the woody cover model prediction performance (coefficient of determination R^2, Root Mean Squared Error (RMSE), Relative Root Mean Square Error (Rel. RMSE) and bias). The model used a random forest algorithm with four dry season FBD ALOS PALSAR images, acquired in 2007, 2008, 2009 and 2010. The models were calibrated with a varying number of samples between 15 and 540, selected using a stratified approach as well as using all LiDAR samples, and further validated with independent equivalent number of samples (also varying from 15 to 540). Models were run 100 times and the error bars indicate one standard deviation of the metric performance.

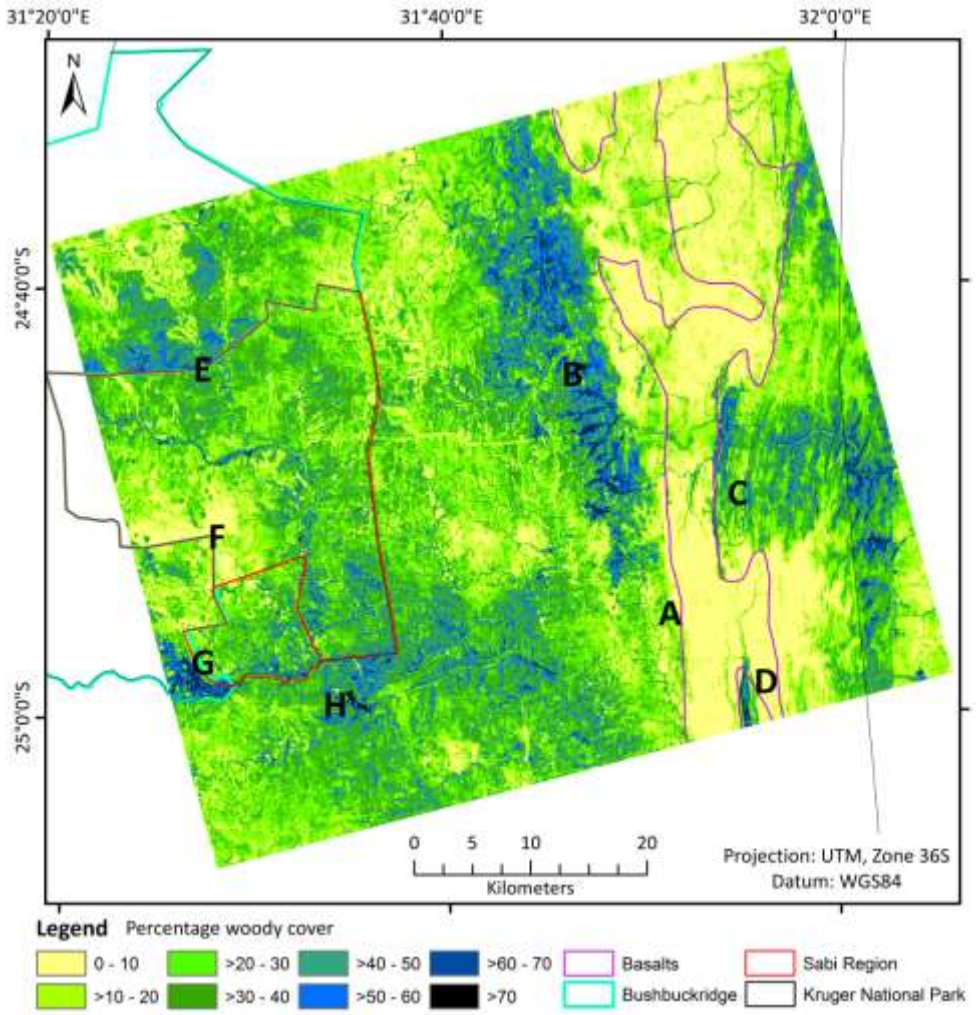

Figure 9: Woody cover map derived from selected PALSAR backscatter intensities at 50 m spatial resolution, overlaid with broad land use classes (Kruger National Park, private Sabi Sands Game Reserve, and communal lands of Bushbuckridge), and basalt substrates. The PALSAR-based woody cover map was produced with a random forest algorithm with dry season images, HH and HV polarization, acquired in 2007, 2008, 2009 and 2010.

4.2.3 Woody cover statistics and spatial patterns

The woody cover map produced with the multi-annual ALOS PALSAR data matches well known patterns in the area. A contrast line between the two main regional geologies (granite vs. gabbro/basalt) is represented as the mark A in Fig. 9. Terrain characteristics and woody cover on both geologies are well expressed in the maps, with the granite landscapes being characterized by more densely wooded hilly terrain with a well-developed drainage network (Levick et al. 2010), and basalt landscape as sparse woodlands with flatter terrain and a weakly developed stream network (Bucini et al. 2010; Wessels et al. 2011). Fine-leaved woodlands with dense thickets (*Acacia welwitschii*) (mark B) also

are observed on the ecca shale geology between the basalts and granites. The dense vegetation patterns occurring in the rocky outcrops of the Lebombo mountains with rhyolite geology (marks C and D) are well identified. On the western side of the image, fence line contrasts associated with diverse land uses and management practices are reflected in the woody vegetation distribution. Two examples are shown at mark E and F. The sector north of the SSGR boundary was, for a few decades, a pasture research station, and maintained a relatively high woody cover through rotational grazing scheme (mark E). The mark F indicates the fence location between SSGR and communal lands dominated by medium density savannas used by the local communities as source of fuel wood and grazing lands. On the private reserve side, historic control of the shrubby layer for improving game viewing led to an open landscape with a few scattered tall trees. Bordering SSGR in the south-west part of the image the mark G corresponds to orchards with dense rows of planted citrus trees. Finally, the mark H shows the main rest camp of KNP, Skukuza, where the high woody cover, compared to surrounding areas, results from irrigation of gardens, fire control and a reduced impact of mega-herbivores (elephants) on trees.

The average woody cover was calculated at 24.2% ± 16.5% in the KNP section of the study area. The average woody cover for the Sabi Sand Game Reserve and the communal lands of the Bushbuckridge Municipality was similar and slightly higher than that of the KNP with 27.9% ± 13.4% and 28.2% ± 15.3% respectively. Despite differences linked to land use and management the east-west cover gradient remains coherent with the increasing mean annual precipitation towards the Drakensberg slopes to the West of the study area. The differences in the distribution of woody vegetation also reflect contrasted geological substrates, especially between granite and basalt/gabbro (Fig. 9) (Bucini et al. 2010; Eckhardt et al. 2000). The average woody cover value in granitic landscapes was 29.4% ± 13.3% while in contrast, woody cover values in basalt/gabbro landscapes were less than 1/3 of this value with an average of 8.1% ± 8.9%. These values are slightly higher than those of Eckhardt et al. (2000), who analyzed aerial photographs along nine transects to estimate woody cover in KNP. The transects were mostly representative of similar vegetation types to our study, essentially Mixed *Combretum* spp./*Terminalia sericea* woodland and *Sclerocarya birrea*/*Acacia nigrescens* savanna

between the Sabie River in the South (southern limit of our ALOS PALSAR images) and the Olifants River in the North (about 60 km North to the northern limit of our ALOS PALSAR images). The study reported for granite and basalt landscapes (photographs taken in 1998) woody cover values ranging between 16.4% and 28.8% (mean 22.1%) and 3.6% and 9.4% (mean 4.3%) on granite and basalt substrates, respectively. We expected our SAR estimates to be higher than Eckhardt's values (assuming no change between 1998 and 2007-2010, this study) since our data are representative of the southern half of the area where most 1998 transects were located and where conditions are generally wetter. We also compared our woody cover estimates with the first wall-to-wall woody cover map for the park produced by Bucini et al. (2010), considering the common extent between our study area and Bucini et al. (2010) KNP map. Bucini's maps was derived from JERS-1 L-band HH SAR and Landsat ETM+ imagery acquired between 1995 and 2001 and was assessed with field data collected in 2006, under the assumption that no major changes would have occurred during this period. Bucini's map produced overall woody cover estimates 12.8% higher than this study (37% vs. 24.2%), 13.2% (42.6% vs. 29.4%) higher when only considering granites and 12.8% (19.9% vs. 8.1%) higher when only considering basalts. These discrepancies could result from differences in datasets and methods used to derive the two products (including the validation protocol), as well as from temporal dynamics in the region, for instance considering the high rate of big tree loss recently reported in the park (Asner and Levick 2012; Levick and Asner 2013). Since both products are based on multi-temporal data with different time span, i.e. 11 year span (1995-2006) in Bucini et al. (2010) and 3 year span (2007-2010) in our study, and with different methods, the inference of temporal dynamics of woody cover was not possible. However, the lower estimates produced by Eckardt et al. (2000) using aerial photographs during a similar period (1998) compared to Bucini's map (1995-2001) may suggest that the latter estimates could generally be overestimated.

5. Conclusion

This work investigated the relationships between satellite-borne ALOS PALSAR L-band data and airborne LiDAR derived woody cover in savanna landscapes of the Kruger National Park region,

South Africa. To the author's knowledge, this is the first comprehensive assessment of the suitability of ALOS PALSAR L-band data for mapping woody cover in these biomes. Discrete-return LiDAR data were used as reference for the calibration and validation of SAR models. Correlation analysis between the two datasets yielded the following conclusions: (1) best relationships were obtained during the dry season, followed by the wet season, and the end of the wet season, (2) co- and cross-polarized backscatters (HH, HV) from the dry season correlated equally well with the reference data, (3) the volume components from polarimetric decompositions (Freeman-Durden, Van Zyl) showed similar correlations to the LiDAR data, when compared to cross-polarized intensities from the same season, (4) relationships improved with the degradation of the scale at which datasets were compared, 50 m was found to be the optimal spatial scale. A multi-annual model was developed using a combination of 2007-2010 dry season HH and HV ALOS PALSAR data for predicting and mapping woody cover. The validation of the woody cover product showed a good relationship between predicted and observed values at a resolution of 50 m with R^2 of 0.71 and RMSE of 7.88%. A woody cover map based on a single SAR acquisition (2008 dry season HH and HV) achieves only a slightly lower accuracy (R^2=0.66, RMSE=8.45%) as multi-annual SAR data, suggesting that a single SAR scene from the dry season can also be used for woody cover mapping. Furthermore, we examined the impact of the number of samples used for model calibration on the model prediction performance. Considering statistical metrics (R^2, RMSE, rRMSE, bias) the SAR-based models achieved stability and robustness of the prediction performance with 180 calibration samples and beyond, which is not common for studies based on field sampling (Fassnacht et al. 2014). The availability of a large number of calibration/validation data was an important advantage. In this study the calibration/validation data covered ca. 3% (11,250 ha) of the total mapped area (365,000 ha). Our investigation showed that L-band backscatter is sensitive to woody cover in savannas and can be used for large-scale mapping in the South African Lowveld. Furterhmore, the study shows that a combination of SAR and LiDAR is relevant for large area mapping, and suggest that the method can be applied to monitor woody cover

changes over entire Kruger National Park, especially bearing in mind new or potentially forthcoming L-band sensors (ALOS-2, DESDynI-R, TanDEM-L, NISAR, SAOCOM).

Acknowledgements

This scientific research is supported by the SANPark Project SARvanna, NRF/BMBF-Project SUA 08/54 and has been undertaken within the framework of the JAXA Kyoto & Carbon Initiative. ALOS PALSAR data have been provided by JAXA EORC. The CSIR team is supported by the Department of Science and Technology, South Africa (grant agreement DST/CON 0119/2010, Earth Observation Application Development in Support of SAEOS), and the European Union's Seventh Framework Programme (FP7/2007-2013, grant agreement no. 282621, AGRICAB). Scientific research in Kruger National Park is supported by the Andrew Mellon Foundation. The Carnegie Airborne Observatory is made possible by the Gordon and Betty Moore Foundation, the Grantham Foundation for the Protection of the Environment, Avatar Alliance Foundation, W. M. Keck Foundation, the Margaret A. Cargill Foundation, Mary Anne Nyburg Baker and G. Leonard Baker Jr., and William R. Hearst III. The authors also thank two anonymous reviewers for their helpful and valuable comments.

References

Antropov, O., Rauste, Y., & Hame, T. (2011). Volume Scattering Modeling in PolSAR Decompositions: Study of ALOS PALSAR Data Over Boreal Forest. *Geoscience and Remote Sensing, IEEE Transactions on, 49*, 3838-3848

Armston, J.D., Denham, R.J., Danaher, T.J., Scarth, P.F., & Moffiet, T.N. (2009). Prediction and validation of foliage projective cover from Landsat-5 TM and Landsat-7 ETM+ imagery. *Journal of Applied Remote Sensing, 3*, 033540-033540-033528

Asner, G.P., Knapp, D.E., Kennedy-Bowdoin, T., Jones, M.O., Martin, R.E., Boardman, J., & Field, C.B. (2007). Carnegie Airborne Observatory: in-flight fusion of hyperspectral imaging and waveform

light detection and ranging for three-dimensional studies of ecosystems. *Journal of Applied Remote Sensing, 1*, 013536-013536-013521

Asner, G.P., & Levick, S.R. (2012). Landscape-scale effects of herbivores on treefall in African savannas. *Ecol Lett, 15*, 1211-1217

Avitabile, V., Baccini, A., Friedl, M.A., & Schmullius, C. (2012). Capabilities and limitations of Landsat and land cover data for aboveground woody biomass estimation of Uganda. *Remote Sensing of Environment, 117*, 366-380

Baccini, A., Laporte, N., Goetz, S.J., Sun, M., & Dong, H. (2008). A first map of tropical Africa's above-ground biomass derived from satellite imagery. *Environmental Research Letters, 3*, 045011

Beale, C.M., Lennon, J.J., Yearsley, J.M., Brewer, M.J., & Elston, D.A. (2010). Regression analysis of spatial data. *Ecol Lett, 13*, 246-264

Beaudoin, A., Le Toan, T., Goze, S., Nezry, E., Lopes, A., Mougin, E., Hsu, C.C., Han, H.C., Kong, J.A., & Shin, R.T. (1994). Retrieval of forest biomass from SAR data. *International Journal of Remote Sensing, 15*, 2777-2796

Breiman, L. (2001). Random Forests. *Machine Learning, 45*, 5-32

Breiman, L., Friedman, J., Stone, C., & Olshen, R.A. (1984). *Classification and Regression Trees (Wadsworth Statistics/Probability)*. Chapman and Hall/CRC

Bucini, G., Hanan, N., P. , Boone, R., B. , Smit, I., P. J. , Saatchi, S., S., Lefsky, M., A., & Asner, G., P. (2010). Woody Fractional Cover in Kruger National Park, South Africa. *Ecosystem Function in Savannas* (pp. 219-237): CRC Press

Buitenwerf, R., Bond, W.J., Stevens, N., & Trollope, W.S.W. (2012). Increased tree densities in South African savannas: >50 years of data suggests CO2 as a driver. *Global Change Biology, 18*, 675-684

Carreiras, J.M.B., Vasconcelos, M.J., & Lucas, R.M. (2012). Understanding the relationship between aboveground biomass and ALOS PALSAR data in the forests of Guinea-Bissau (West Africa). *Remote Sensing of Environment, 121*, 426-442

Cartus, O., Kellndorfer, J., Rombach, M., & Walker, W. (2012). Mapping Canopy Height and Growing Stock Volume Using Airborne Lidar, ALOS PALSAR and Landsat ETM+. *Remote Sensing, 4*, 3320-3345

Castel, T., Beaudoin, A., Stach, N., Stussi, N., Le Toan, T., & Durand, P. (2001). Sensitivity of space-borne SAR data to forest parameters over sloping terrain. Theory and experiment. *International Journal of Remote Sensing, 22*, 2351-2376

Chauhan, N.S., Lang, R.H., & Ranson, K.J. (1991). Radar modeling of a boreal forest. *Geoscience and Remote Sensing, IEEE Transactions on, 29*, 627-638

Cho, M.A., Mathieu, R., Asner, G.P., Naidoo, L., van Aardt, J., Ramoelo, A., Debba, P., Wessels, K., Main, R., Smit, I.P.J., & Erasmus, B. (2012). Mapping tree species composition in South African savannas using an integrated airborne spectral and LiDAR system. *Remote Sensing of Environment, 125*, 214-226

Coughenour, M.B., & Ellis, J.E. (1993). Landscape and Climatic Control of Woody Vegetation in a Dry Tropical Ecosystem: Turkana District, Kenya. *Journal of Biogeography, 20*, 383-398

Dong, J., Xiao, X., Sheldon, S., Biradar, C., Zhang, G., Dinh Duong, N., Hazarika, M., Wikantika, K., Takeuhci, W., & Moore, B., III (2014). A 50-m Forest Cover Map in Southeast Asia from ALOS/PALSAR and Its Application on Forest Fragmentation Assessment. *PLoS One, 9*

Eckhardt, H.C., van Wilgen, B.W., & Biggs, H.C. (2000). Trends in woody vegetation cover in the Kruger National Park, South Africa, between 1940 and 1998. *African Journal of Ecology, 38*, 108-115

Englhart, S., Keuck, V., & Siegert, F. (2011). Aboveground biomass retrieval in tropical forests — The potential of combined X- and L-band SAR data use. *Remote Sensing of Environment, 115*, 1260-1271

Fassnacht, F.E., Hartig, F., Latifi, H., Berger, C., Hernández, J., Corvalán, P., & Koch, B. (2014). Importance of sample size, data type and prediction method for remote sensing-based estimations of aboveground forest biomass. *Remote Sensing of Environment, 154*, 102-114

Ferrazzoli, P., & Guerriero, L. (1995). Radar sensitivity to tree geometry and woody volume: a model analysis. *Geoscience and Remote Sensing, IEEE Transactions on, 33*, 360-371

Freeman, A., & Durden, S.L. (1998). A three-component scattering model for polarimetric SAR data. *Geoscience and Remote Sensing, IEEE Transactions on, 36*, 963-973

GAMMA (2008). Differential Interferometry and Geocoding Software - DIFF&GEO. Geocoding and image regristration. In R.S. GAMMA (Ed.), *Documentation - User's Guide*

Hansen, M.C., Townshend, J.R.G., DeFries, R.S., & Carroll, M. (2005). Estimation of tree cover using MODIS data at global, continental and regional/local scales. *International Journal of Remote Sensing, 26*, 4359-4380

Jennings, S., Brown, N., & Sheil, D. (1999). Assessing forest canopies and understorey illumination: canopy closure, canopy cover and other measures. *Forestry, 72*, 59-74

Kasischke, E.S., Melack, J.M., & Dobson, M.C. (1997). The use of imaging radars for ecological applications - A review. *Remote Sensing of Environment, 59*, 141-156

Kulmatiski, A., & Beard, K.H. (2013). Woody plant encroachment facilitated by increased precipitation intensity. *Nature Clim. Change, 3*, 833-837

Le Toan, T., Beaudoin, A., Riom, J., & Guyon, D. (1992). Relating Forest Biomass to Sar Data. *Ieee Transactions on Geoscience and Remote Sensing, 30*, 403-411

Leckie, D.G., & Ranson, K.J. (1996). Forestry applications using imaging radar. In F.M. Henderson, & A.J. Lewis (Eds.), *Principles & Applications of Imaging Radar. Manual of Remote Sensing* (pp. 435-509)

Lee, J.-S., & Pottier, E. (2009). *Polarimetric radar imaging: from basics to applications*. CRC press

Lefsky, M.A., Cohen, W.B., Parker, G.G., & Harding, D.J. (2002). Lidar Remote Sensing for Ecosystem Studies. *BioScience, 52,* 19-30

Lehmann, E.A., Wallace, J.F., Caccetta, P.A., Furby, S.L., & Zdunic, K. (2013). Forest cover trends from time series Landsat data for the Australian continent. *International Journal of Applied Earth Observation and Geoinformation, 21*, 453-462

Levick, S.R., & Asner, G.P. (2013). The rate and spatial pattern of treefall in a savanna landscape. *Biological Conservation, 157,* 121-127

Levick, S.R., Asner, G.P., Chadwick, O.A., Khomo, L.M., Rogers, K.H., Hartshorn, A.S., Kennedy-Bowdoin, T., & Knapp, D.E. (2010). Regional insight into savanna hydrogeomorphology from termite mounds. *Nat Commun, 1,* 65

Li, S., Potter, C., Hiatt, C., & Shupe, J. (2012). Fusion of Hyperspectral and L-Band SAR Data to Estimate Fractional Vegetation Cover in a Coastal California Scrub Community. *Journal of Geophysics and Remote Sensing*

Loveland, T.R., Reed, B.C., Brown, J.F., Ohlen, D.O., Zhu, Z., Yang, L., & Merchant, J.W. (2000). Development of a global land cover characteristics database and IGBP DISCover from 1 km AVHRR data. *International Journal of Remote Sensing, 21*, 1303-1330

Lu, D. (2006). The potential and challenge of remote sensing‐based biomass estimation. *International Journal of Remote Sensing, 27*, 1297-1328

Lucas, R.M., Cronin, N., Moghaddam, M., Lee, A., Armston, J., Bunting, P., & Witte, C. (2006). Integration of radar and Landsat-derived foliage projected cover for woody regrowth mapping, Queensland, Australia. *Remote Sensing of Environment, 100*, 388-406

Lucas, R.M., Moghaddam, M., & Cronin, N. (2004). Microwave scattering from mixed-species forests, Queensland, Australia. *Geoscience and Remote Sensing, IEEE Transactions on, 42*, 2142-2159

Main, R., Mathieu, R., Kleynhans, W., Wessels, K., Naidoo, L., & Asner, G.P. (2014). Woody cover assessments in a Southern African savanna, using hyper-temporal C-band ASAR-WS data. In, *IEEE International Geoscience and Remote Sensing Symposium (IGARSS) 2014* (pp. 1148-1151)

Marchant, R. (2010). Understanding complexity in savannas: climate, biodiversity and people. *Current Opinion in Environmental Sustainability, 2*, 101-108

Mathieu, R., Naidoo, L., Cho, M.A., Leblon, B., Main, R., Wessels, K., Asner, G.P., Buckley, J., Van Aardt, J., Erasmus, B.F.N., & Smit, I.P.J. (2013). Toward structural assessment of semi-arid African savannahs and woodlands: The potential of multitemporal polarimetric RADARSAT-2 fine beam images. *Remote Sensing of Environment, 138*, 215-231

Mitchard, E.T.A., Saatchi, S.S., Woodhouse, I.H., Nangendo, G., Ribeiro, N.S., Williams, M., Ryan, C.M., Lewis, S.L., Feldpausch, T.R., & Meir, P. (2009). Using satellite radar backscatter to predict above-ground woody biomass: A consistent relationship across four different African landscapes. *Geophysical Research Letters, 36*

Montesano, P.M., Nelson, R., Sun, G., Margolis, H., Kerber, A., & Ranson, K.J. (2009). MODIS tree cover validation for the circumpolar taiga-tundra transition zone. *Remote Sensing of Environment, 113*, 2130-2141

Musick, H.B., Schaber, G.S., & Breed, C.S. (1998). AIRSAR studies of woody shrub density in semiarid rangeland: Jornada del Muerto, New Mexico. *Remote Sensing of Environment, 66*, 29-40

Oliver, C., & Quegan, S. (2004). *Understanding Synthetic Aperture Radar Images*. SciTech Publ.

Raney, R.K. (1996). Radar fundamentals: technical perspective. In F.M. Henderson, & A.J. Lewis (Eds.), *Principles & Applications of Imaging Radar. Manual of Remote Sensing* (pp. 9-130)

Rauste, Y., Hame, T., Pulliainen, J., Heiska, K., & Hallikainen, M. (1994). Radar-based forest biomass estimation. *International Journal of Remote Sensing, 15*, 2797-2808

Rignot, E.J.M., Williams, C.L., Way, J.B., & Viereck, L.A. (1994). Mapping of Forest Types in Alaskan Boreal Forests Using Sar Imagery. *Ieee Transactions on Geoscience and Remote Sensing, 32*, 1051-1059

Rosenqvist, A., Shimada, M., & Watanabe, M. (2004). ALOS PALSAR: Technical outline and mission concepts. In, *4th International Symposium on Retrieval of Bio- and Geophysical Parameters from SAR Data for Land Applications*. Innsbruck, Austria

Ryan, C.M., Hill, T., Woollen, E., Ghee, C., Mitchard, E., Cassells, G., Grace, J., Woodhouse, I.H., & Williams, M. (2012). Quantifying small-scale deforestation and forest degradation in African woodlands using radar imagery. *Global Change Biology, 18*, 243-257

Saatchi, S., Marlier, M., Chazdon, R.L., Clark, D.B., & Russell, A.E. (2011). Impact of spatial variability of tropical forest structure on radar estimation of aboveground biomass. *Remote Sensing of Environment, 115*, 2836-2849

Sankaran, M., Hanan, N.P., Scholes, R.J., Ratnam, J., Augustine, D.J., Cade, B.S., Gignoux, J., Higgins, S.I., Le Roux, X., Ludwig, F., Ardo, J., Banyikwa, F., Bronn, A., Bucini, G., Caylor, K.K., Coughenour, M.B., Diouf, A., Ekaya, W., Feral, C.J., February, E.C., Frost, P.G.H., Hiernaux, P., Hrabar, H., Metzger, K.L., Prins, H.H.T., Ringrose, S., Sea, W., Tews, J., Worden, J., & Zambatis, N. (2005). Determinants of woody cover in African savannas. *Nature, 438*, 846-849

Sankaran, M., Ratnam, J., & Hanan, N.P. (2004). Tree–grass coexistence in savannas revisited – insights from an examination of assumptions and mechanisms invoked in existing models. *Ecol Lett, 7*, 480-490

SANParks (2013a). Kruger National Park weather and rainfall data 2009 until present. In SANParks (Ed.). http://dataknp.sanparks.org/sanparks/metacat/judithk.1056.5/sanparks

SANParks (2013b). Kruger National Park weather and rainfall data (pre 1960-2008). In SANParks (Ed.). http://dataknp.sanparks.org/sanparks/metacat/judithk.609.30/sanparks

Santoro, M., Beer, C., Cartus, O., Schmullius, C., Shvidenko, A., McCallum, I., Wegmüller, U., & Wiesmann, A. (2011). Retrieval of growing stock volume in boreal forest using hyper-temporal series of Envisat ASAR ScanSAR backscatter measurements. *Remote Sensing of Environment, 115*, 490-507

Scholes, R.J., & Archer, S.R. (1997). Tree-Grass Interactions In Savannas. *Annual Review of Ecology and Systematics, 28*, 517-544

Shimada, M., Itoh, T., Motooka, T., Watanabe, M., Shiraishi, T., Thapa, R., & Lucas, R. (in press). New global forest/non-forest maps from ALOS PALSAR data (2007–2010). *Remote Sensing of Environment*

Singh, G., Yamaguchi, Y., & Park, S.E. (2013). General Four-Component Scattering Power Decomposition With Unitary Transformation of Coherency Matrix. *Geoscience and Remote Sensing, IEEE Transactions on, 51*, 3014-3022

Smit, I.P.J., Smit, C.F., Govender, N., Linde, M.v.d., & MacFadyen, S. (2013). Rainfall, geology and landscape position generate large-scale spatiotemporal fire pattern heterogeneity in an African savanna. *Ecography, 36*, 447-459

Stussi, N., Beaudoin, A., Castel, T., & Gigord, P. (1995). Radiometric correction of multi-configuration spaceborne SAR data over hilly terrain. In, *1st International Workshop on Retrieval of Bio- and Geophysical Parameters from SAR data for Land Applications*. Toulouse, France

van Zyl, J.J. (1989). Unsupervised classification of scattering behavior using radar polarimetry data. *Geoscience and Remote Sensing, IEEE Transactions on, 27*, 36-45

van Zyl, J.J., Yunjin, K., & Arii, M. (2008). Requirements for Model-based Polarimetric Decompositions. In, *Geoscience and Remote Sensing Symposium, 2008. IGARSS 2008. IEEE International* (pp. V - 417-V - 420)

Venter, F.J., Scholes, R.J., & Eckhardt, H.C. (2003). The abiotic and template its associated vegetation pattern. In J.T. Du Toit, K.H. Rogers, & H.C. Biggs (Eds.), *The Kruger Experience. Ecology and Management of Savanna Heterogeneity*: London Island Press

Watanabe, M., Shimada, M., Rosenqvist, A., Tadono, T., Matsuoka, M., Shakil Ahmad, R., Ohta, K., Furuta, R., Nakamura, K., & Moriyama, T. (2006). Forest Structure Dependency of the Relation Between L-Band σ0 and Biophysical Parameters. *Geoscience and Remote Sensing, IEEE Transactions on, 44*, 3154-3165

Wentao, A., Yi, C., & Jian, Y. (2010). Three-Component Model-Based Decomposition for Polarimetric SAR Data. *Geoscience and Remote Sensing, IEEE Transactions on, 48*, 2732-2739

Wessels, K.J., Mathieu, R., Erasmus, B.F.N., Asner, G.P., Smit, I.P.J., van Aardt, J.A.N., Main, R., Fisher, J., Marais, W., Kennedy-Bowdoin, T., Knapp, D.E., Emerson, R., & Jacobson, J. (2011). Impact of communal land use and conservation on woody vegetation structure in the Lowveld savannas of South Africa. *Forest Ecology and Management, 261*, 19-29

Yamaguchi, Y., Moriyama, T., Ishido, M., & Yamada, H. (2005). Four-component scattering model for polarimetric SAR image decomposition. *Geoscience and Remote Sensing, IEEE Transactions on, 43*, 1699-1706

Yamaguchi, Y., Sato, A., Boerner, W.M., Sato, R., & Yamada, H. (2011). Four-Component Scattering Power Decomposition With Rotation of Coherency Matrix. *Geoscience and Remote Sensing, IEEE Transactions on, 49*, 2251-2258

Zeidler, J., Wegmann, M., & Dech, S. (2012). Spatio-temporal robustness of fractional cover upscaling: a case study in semi-arid Savannah's of Namibia and Western Zambia. In, *SPIE, Earth Resources and Environmental Remote Sensing/GIS Applications III*. Edinburgh, United Kingdom